Arctic Science

OPEN ACCESS | Article

Evolution of the dynamics of Airdrop Glacier, western Axel Heiberg Island, over a seven-decade-long advance

Benoît Lauzon[a], **Luke Copland**[a], **Wesley Van Wychen**[a,b], **William Kochtitzky**[c], **and Robert McNabb**[d]

[a]Department of Geography, Environment and Geomatics, University of Ottawa, Ottawa, ON, Canada; [b]Department of Geography and Environmental Management, University of Waterloo, Waterloo, ON, Canada; [c]School of Marine and Environmental Programs, University of New England, Biddeford, ME, USA; [d]School of Geography and Environmental Sciences, Ulster University, Coleraine, United Kingdom

Corresponding author: **Benoît Lauzon** (email: blauz052@uottawa.ca)

Abstract

Various remotely sensed data, including historical aerial photographs, declassified intelligence satellite photographs, optical satellite imagery, and synthetic aperture radar data, were used to undertake the first comprehensive reconstruction of the dynamics of Airdrop Glacier on Axel Heiberg Island, Nunavut. Observations show a continuous terminus advance totalling ~6 km since 1950 and notably less variability in its surface velocities in comparison to adjacent Iceberg Glacier. This advance is concurrent with relatively high flow rates over its entire surface, resulting in significant thickening near the terminus and thinning at higher elevations. Velocities have more than halved from the mid-2000s to 2021, but without any definitive evidence of previous flow instabilities, we cannot confirm whether Airdrop's behaviour is cyclic in nature and therefore characteristic of a surge. Instead, Airdrop Glacier could be experiencing a delayed response to the positive mass balance conditions of the Little Ice Age, which could also explain the advance of other nearby glaciers. Its recent slowdown could then be indicative of a gradual adjustment to recent climatic conditions. This study highlights the need for comprehensive studies of glacier dynamics in the Canadian Arctic to improve our understanding of the factors triggering dynamic instabilities and causing the observed variety of behaviours.

Key words: glacier dynamics, glacier surging, remote sensing, Axel Heiberg Island, Canadian Arctic

1. Introduction

With amplified climate warming in the Arctic, monitoring glacier dynamics is critical to understanding the fundamental processes that drive glacier flow and how these may be affected by a warming climate. Glaciers in the Canadian Arctic Archipelago (CAA; Ellesmere, Axel Heiberg, and Devon islands) demonstrate a high degree of spatial and temporal variability in their dynamics. The negative mass balance conditions that have prevailed in this region during the last few decades (Koerner 2005; Gardner et al. 2011; Lenaerts et al. 2013; Millan et al. 2017; Thomson et al. 2017; Mortimer et al. 2018; Noël et al. 2018; Ciracì et al. 2020) have been accompanied by widespread terminus retreat, lower ice velocities, and glacier thinning (Schaffer et al. 2017; Strozzi et al. 2017; Thomson and Copland 2017; Thomson et al. 2017; Mortimer et al. 2018; Kochtitzky and Copland 2022). Nevertheless, some large tidewater glaciers, such as Trinity, Wykeham, and Belcher glaciers, have undergone a dramatic acceleration because of dynamic thinning (Van Wychen et al. 2016, 2017; Harcourt et al. 2020; Dalton et al. 2022). Moreover, other tidewater glaciers have experienced marked interannual velocity variations, accompanied by changes in their terminus position and ice thickness (Van Wychen et al. 2014, 2016). Several tidewater glaciers in the Canadian Arctic also go through pulse-like variations in their velocities but lack sufficient evidence to confidently classify them as surge-type glaciers (Van Wychen et al. 2016, 2017). Flow variability for these glaciers is typically restricted to the lowermost terminus regions that are grounded below sea level, with the up-glacier propagation of the pulse appearing to be limited by where bed elevations rise above sea level (a.s.l.). Tidewater dynamics and bedrock geography are also thought to contribute to surge initiation at or near the terminus of several glaciers in Svalbard (Rolstad et al. 1997; Luckman et al. 2002; Dowdeswell and Benham 2003; Murray et al. 2003, 2012; Dunse et al. 2015; Flink et al. 2015; Sevestre et al. 2018) and of Iceberg Glacier in the Canadian Arctic (Lauzon et al. 2023).

Despite this region being outside of the optimal climatic envelope for surging suggested by Sevestre and Benn (2015), more than 50 surge-type glaciers have been identified in the Canadian Arctic (Copland et al. 2003; Sevestre and Benn 2015). The most significant terminus advances out of the 51 surge-type glaciers inventoried by Copland et al. (2003) in the CAA occurred on western Axel Heiberg Island, in the northern CAA. The only glaciers defined as "confirmed" surge-type

out of 13 with signs of unstable flow on Axel Heiberg Island were the three largest, namely Airdrop, Iceberg, and Good Friday (Copland et al. 2003). Iceberg, Airdrop, and Good Friday glaciers underwent 4.5, 5, and 7 km of terminus advance from 1959 to 1999, respectively (Copland et al. 2003). The dynamics of Iceberg and Good Friday glaciers have been analyzed in detail in previous studies, demonstrating starkly different behaviours between the two tidewater glaciers, as Good Friday Glacier has been experiencing an uninterrupted terminus advance over more than seven decades while Iceberg Glacier exhibits typical surging patterns (Medrzycka et al. 2019; Lauzon et al. 2023). Conversely, no thorough investigations into the behaviour of Airdrop Glacier have been undertaken in the existing literature.

The aim of this study is to improve our understanding of the complex behaviour and dynamics of glaciers in the Canadian Arctic by reconstructing the changes of Airdrop Glacier from 1950 to 2021. The terminus of this glacier is significantly more advanced now than it was in 1959 (Copland et al. 2003; Van Wychen et al. 2016), but the details of the timing of this advance along with the associated changes in ice motion and surface elevation are currently poorly constrained, and it is unclear whether the advance can be best explained by surging or another mechanism. Our assessment is undertaken by utilizing a wide array of remotely sensed data, such as historical aerial photographs, declassified intelligence satellite photographs, optical satellite imagery, and synthetic aperture radar (SAR) data.

2. Study site

More than a quarter of Axel Heiberg Island's total land area of 43,000 km^2 is covered by glaciers, with Steacie Ice Cap in the south and Müller Ice Cap in the north (Ommanney 1969; Thomson et al. 2011). This region has a cold and dry climate with mean annual temperatures of about −20° C and mean annual precipitation ranging from 58 mm a^{-1} at sea level measured at Eureka, 100 km to the east (Fig. 1), to 370 mm a^{-1} at 2120 m a.s.l. (Cogley et al. 1996*a*; Thomson et al. 2017). The surface motion in the interior of the two ice caps on Axel Heiberg, where most of the ice is frozen to its bed and flowing due to internal deformation alone, remains below 20 m a^{-1} (Van Wychen et al. 2016). As the ice is channelled downglacier towards glacier termini, which raises the potential for a transition from cold to warm basal conditions, as well as changes in bedrock topography (sills and steps), velocities typically increase along the main trunk of outlet glaciers (Van Wychen et al. 2016). Surface velocities of land-terminating glaciers generally remain below 75 m a^{-1}, with the two only exceptions being Airdrop Glacier and the upper half of Thompson Glacier (Van Wychen et al. 2016, 2021), which both discharge to the west of Müller Ice Cap (Fig. 1). Müller Ice Cap's sole marine-terminating glacier, Iceberg Glacier, is currently stagnant along its main trunk (<20 m a^{-1}), but its tributaries have velocities of up to ∼75 m a^{-1} (Van Wychen et al. 2021), and terminus velocities reached >2000 m a^{-1} during a surge between the early 1980s and 2003 (Lauzon et al. 2023). On the other hand, Good Friday Glacier, the only marine-terminating glacier draining Steacie Ice Cap, currently has flow rates of 100–250 m a^{-1} along its main trunk and >350 m a^{-1} at the terminus (Medrzycka et al. 2019).

Airdrop Glacier (79.84°N, 93.28°W; Fig. 1) is a land-terminating glacier with a total basin size of ∼600 km^2 that drains the west side of Müller Ice Cap. This glacier was first identified as a surge-type glacier by Copland et al. (2003). "Airdrop Glacier" is an unofficial name and is used interchangeably with "Middle Glacier" since the glacier feeds Middle Fiord. The glacier had surface features indicative of glacier surging in both 1959 and 1999, with extensive surface folding and looping of surface moraines apparent in both years and intense crevassing in 1999 satellite imagery (Copland et al. 2003). The glacier had advanced by ∼4.5 km between 1959 and 1999 and saw an 18.45 km^2 increase in its area from 1959 to 2000 (Thomson et al. 2011). In the year 2000, the glacier had a velocity of ∼150–180 m a^{-1} and was determined to have had a latest surge initiation in 1975 (Thomson et al. 2011). According to a subsequent study by Van Wychen et al. (2016), Airdrop Glacier advanced by a further ∼1 km from 2000 to 2014 and reduced in flow rate from 165 m a^{-1} in 2000 to 75 m a^{-1} in 2015, with peak velocities in the lower half of the glacier. The authors argued that this slowdown could be indicative of a transition to the quiescent phase of the surge cycle.

3. Materials and methods

3.1. Terminus position

A total of 43 historical aerial photographs, declassified spy satellite images, optical satellite images, and SAR scenes were used to manually outline the terminus position of Airdrop Glacier from 1959 to 2021 (Table 1) in ArcGIS 10.8.1 and quantify terminus changes over the study period. Nadir and oblique historical aerial photographs from 1950 and 1959 were acquired from the National Air Photo Library (NAPL), Ottawa, Canada. The 1950 photos were acquired by the Royal Canadian Air Force (RCAF) during a trimetrogon survey (i.e., one camera pointing nadir and two pointing to either side of the flight path) at an altitude of 19,500–22,000 ft (5944–6706 m) a.s.l., with each nadir image covering a ground area of ∼14 km × 14 km (Cogley and Adams 2000). The 1959 survey acquired nadir images at an altitude of ∼30,000 ft (∼9000 m) a.s.l., which were used by Ommanney (1969) to create the first inventory of Axel Heiberg Island's ice masses. Pairs of declassified spy satellite photographs from the KH-4 Corona KH-9 Hexagon Cold War era reconnaissance satellite from 1966 and 1977, respectively, were downloaded from the United States Geological Survey (USGS) Earth Explorer data portal (http://earthexplorer.usgs.gov). These were acquired in stereoscopic (stereo) mode and provide a ground resolution of approximately 4.7 and 8.0 m, respectively.

For the purpose of terminus delineation, the scanned historical aerial photographs and declassified spy satellite images were cropped to the terminus region of Airdrop Glacier and manually georeferenced using recent Landsat 8 images as a reference and a first-order polynomial (affine) transfor-

Fig. 1. (*a*) Location of Airdrop Glacier, Iceberg Glacier, White Glacier, Thompson Glacier, and Good Friday Glacier on Axel Heiberg Island, Nunavut. (*b*) Airdrop Glacier centreline (red line) and 5 km markers starting from the glacier's 2018 terminus position. Base image: Landsat 8, 12 August 2020. Data: Statistics Canada, 2016 Census. Provinces/territories—Cartographic Boundary File (https://www12.statcan.gc.ca/censusrecensement/2011/geo/bound-limit/bound-limit-2016-eng.cfm). Natural Resources Canada. Lakes, Rivers and Glaciers in Canada—CanVec Series—Hydrographic Features (https://open.canada.ca/data/en/dataset/9d96e8c9-22fe-4ad2-b5e8-94a6991b744b).

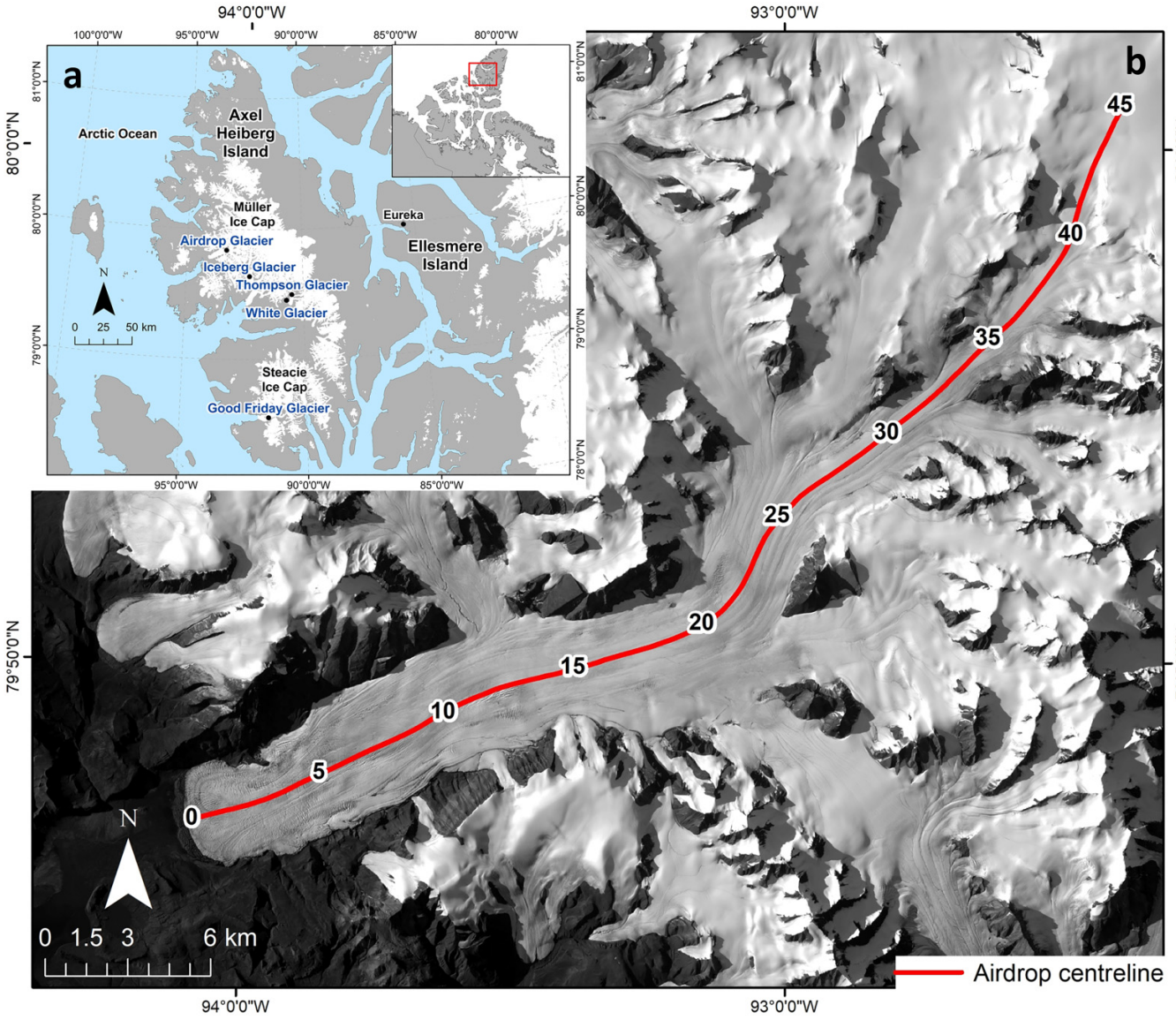

mation with a minimum of eight tie points in ArcGIS. The 1959 and 1966 outlines were delineated using a historical aerial photograph and a KH-4 Corona declassified spy image, respectively (Table 1). When comparing the location of fixed bedrock features near the glacier terminus, an offset of ~50 m was found between the 1959 georeferenced historical aerial photograph and the 1966 georeferenced KH-4 image, and an offset of ~50 m was calculated between the 1966 georeferenced KH-4 image and the 1972 Landsat 1 image. No 1950 nadir air photographs covered the terminus of Airdrop, so non-georeferenced oblique photos of the terminus from that year were used to determine its approximate position in relation to the 1959 position.

All the terminus positions since 1972 were mapped using satellite imagery, the majority of which was optical (Table 1). This imagery consists of Landsat 1–8 Level 1TP (i.e., precision and terrain corrected) scenes obtained from the USGS Earth Explorer data portal (http://earthexplorer.usgs.gov) and Advanced Spaceborne Emission and Reflection Radiometer (ASTER) L1T (i.e., calibrated-at-sensor radiance that is geometrically corrected and projected in UTM coordinates) acquired from the USGS Earth Explorer data portal, NASA's Earthdata search portal (https://search.earthdata.nasa.gov/search), and the METI AIST Data Archive System (https://gbank.gsj.jp/madas/map/index.html). When available, July to September (i.e., late summer) images were

Table 1. Imagery used for mapping the terminus positions of Airdrop Glacier in this study.

Acquisition date	Image ID	Resolution (m)	Satellite/photographer
16/07/1950	T412L-120	–	RCAF
28/07/1959	A16754_053	~5.7	RCAF
14/08/1966	DS1036-1082DF023_d	~4.7	KH-4 Corona
28/08/1972	LM01L1T06200219720828	60	Landsat 1
23/05/1973	LM01L1T06300219730526	60	Landsat 1
19/08/1974	LM01L1TP06300219740819	60	Landsat 1
24/07/1975	LM02L1TP06900119750724	60	Landsat 2
22/09/1976	LM02L1TP06300219760922	60	Landsat 2
29/08/1977	LM02L1TP06200219770829	60	Landsat 2
03/09/1978	LM03L1TP06300219780903	60	Landsat 3
29/07/1979	LM03L1TP06800119790729	60	Landsat 3
19/09/1980	LM02L1TP06300219800919	60	Landsat 3
30/08/1981	LM02L1TP06600219810830	60	Landsat 2
09/08/1991	LT05L1TP05300319910809	30	Landsat 5
05/11/1992	E1_06833_STD_F203	12.5	ERS-1
06/11/1993	E1_12072_STD_F203	12.5	ERS-1
07/10/1994	E1_16876_STD_F203	12.5	ERS-1
29/09/1995	LT05L1TP06100219950929	30	Landsat 5
29/10/1996	R1_05151_ST6_F199	12.5	RADARSAT-1
07/11/1997	E2_13327_STD_F203	12.5	ERS-2
24/03/1998	E2_15288_STD_F203	12.5	ERS-2
25/07/1999	LE07L1TP05800219990725	15	Landsat 7
29/09/2000	LE07L1TP05600220000729	15	Landsat 7
26/06/2001	LE07L1TP06000220010626	15	Landsat 7
12/06/2002	LE07L1TP05800220020615	15	Landsat 7
11/07/2003	AST_L1T_00307112003202307	15	ASTER
20/07/2004	AST_L1T_00307202004003948	15	ASTER
29/07/2005	AST_L1T_00307292005195221	15	ASTER
09/07/2006	AST_L1T_00307092006013457	15	ASTER
15/08/2007	AST_L1T_00308152007193453	15	ASTER
02/07/2008	LT05L1TP05700220080702	30	Landsat 5
16/07/2009	LT05L1TP05400320090716	30	Landsat 5
05/07/2010	AST_L1B_00307052010004005	15	ASTER
23/07/2011	AST_L1T_00309232011195817	15	ASTER
20/07/2012	AST_L1T_00309202012194021	15	ASTER
14/09/2013	LC08L1TP06100220130914	15	Landsat 8
12/08/2014	LC08L1TP09024220140812	15	Landsat 8
01/09/2015	LC08L1TP05600220150901	15	Landsat 8
29/07/2016	LC08L1TP06000220160729	15	Landsat 8
28/08/2017	LC08L1TP05700220170828	15	Landsat 8
21/08/2018	LC08L1TP09224120180821	15	Landsat 8
19/09/2019	LC08L1TP05700220190919	15	Landsat 8
07/08/2020	LC08L1TP08724220200807	15	Landsat 8
15/08/2021	LC08L1TP09024220210815	15	Landsat 8

preferentially chosen to ensure minimal snow cover and sea ice. The Landsat and ASTER scenes were all radiometrically/geometrically corrected, and thus no pre-processing was required.

The SAR data used for the terminus analysis consists of several European Remote-Sensing Satellite (ERS) 1 and 2 scenes for the period 1991–2011, along with a single 1996 RADARSAT-1 scene, obtained from the Alaska Satellite Facility Data Search portal (https://search.asf.alaska.edu). The SAR data were downloaded as Level 1 (i.e., processed) products and geocoded to NAD 1983 Zone 15 N with the ASF MapReady software to create a GeoTIFF file of each scene. Some of the ERS scenes were not accurately georeferenced and, therefore, had to be manually adjusted using the Shift tool from the Georeferencing toolbar in ArcGIS to properly align bedrock features in the terminus region with the same features in recent Landsat 8 scenes. These corrections ranged from about 65–120 m (5.4–9.6 pixels). Due to the limited high-latitude coverage of

Table 2. Landsat (L) and ERS scene pairs used to derive surface velocities of Airdrop Glacier, with associated error quantified by the median apparent motion over adjacent non-glacierized terrain and uncertainty determined by the standard deviation over the same area.

Satellite	First scene	Second scene	Error (m a^{-1})	Uncertainty (m a^{-1})
L1	23/09/1972	12/09/1974	17.3	12.5
L1/L2	19/08/1974	06/08/1975	34.9	24.2
L2	10/09/1975	04/09/1976	38.3	28.5
L2	03/08/1976	29/07/1977	55.8	27.3
L2	12/07/1977	04/07/1978	18.2	16.8
L2/L3	03/09/1978	07/09/1979	34.4	22.8
L2	07/09/1979	19/09/1980	43.2	29.9
L2	19/09/1980	30/08/1981	26.8	24.7
ERS-1	06/02/1992	07/03/1992	23.8	15.9
ERS-2	08/04/1997	13/05/1997	14.5	18.2
L7	20/07/1999	20/06/2000	5.0	4.5
L7	11/06/2000	14/06/2001	6.0	5.0
L7	15/06/2001	18/06/2002	7.0	6.7
L7	15/06/2004	02/06/2005	4.0	4.2
L7	09/06/2005	14/07/2006	4.0	43.2
L8	05/05/2019	07/05/2020	5.0	4.5
L8	11/05/2020	14/05/2021	3.0	4.0

the early Landsat satellites, the ERS imagery was used to fill some data gaps in the 1990s (Table 1). Unfortunately, no imagery was available from 1982 to 1991.

Total and mean annual changes in terminus position were quantified along Airdrop Glacier's centreline for different periods: 1959–1966, 1966–1972, 1972–1981, 1981–1991, 1991–2000, 2000–2010, and 2010–2021. Errors from manual delineation of terminus extents are generally within one pixel (Paul et al. 2013); however, we have conservatively estimated the maximum uncertainty to be two pixels (Kochtitzky et al. 2019) to account for variations in the georeferencing and orthorectification accuracy of the satellite imagery that were not corrected by manual shifting. This translates to a total uncertainty of 120 m for Landsat 1–3, 60 m for Landsat 4–5, 30 m for Landsat 7–8, 25 m for ERS-1/2 and RADARSAT-1, ~11.4 m for the 1959 historical aerial photograph, and ~9.4 m for the 1966 KH-4 image. Because the manual georeferencing of the 1959 historical aerial photograph and 1966 KH-4 Corona image introduced additional uncertainty in the glacier terminus position changes calculated from these images, the offsets between the 1959, 1966, and 1972 images were added to the numerator of eq. 1 for the 1959–1966 and 1966–1972 time periods. For time periods that include imagery from sensors with different resolutions, the average resolution is taken when calculating uncertainties for terminus advance rates. With the assumption that uncertainties are caused by random error (i.e., independent from one another) and there is no systematic bias, uncertainties for the mean annual terminus position change rate of Airdrop Glacier over the different time periods were calculated from:

$$\text{Uncertainty} = \frac{\sqrt{2\left(\text{pixel size}^2\right)}}{\text{number of years}} \quad (1)$$

3.2. Ice velocities

Changes in the flow rate of Airdrop Glacier between 1972 and 2021 were computed from a variety of different satellite sensors, which allows for the analysis of temporal variability in ice flow to determine whether there is evidence of a dynamic instability, such as a glacier surge, in the available velocity record.

3.2.1. Glacier image velocimetry

Velocities from 1972 to 1981 were extracted from Landsat 1–3 imagery using the glacier image velocimetry (GIV) app (Van Wyk de Vries 2021a, 2021b; Van Wyk de Vries and Wyckert 2021). GIV, like most other software used to derive glacier motion, uses a feature-tracking algorithm that matches offsets by finding corresponding features or image patches in two or more images (Debella-Gilo and Kääb 2011). The measurement of the displacement of features between images over a specific time interval is used to compute ice surface velocities. Landsat 1–3 near-annually separated satellite images with a matching orbital geometry (i.e., same path and row) were clipped to Airdrop Glacier and its immediate surroundings before inputting the data into GIV. A signal-to-noise ratio of 5 and a search window size of 30 × 30 pixels were used for each image pair. Due to slightly inaccurate georeferencing of some of the early Landsat images, the 03/09/1978 and 30/08/1981 scenes (Table 2) had to be manually shifted, as described in Section 3.1, by a total of 40 and 60 m, respectively. The coarse resolution of these early Landsat images also resulted in larger errors and uncertainties compared to velocities derived from more recent, higher resolution imagery (Table 2). The uncertainty calculations for the velocities are described later in this section.

Once the surface velocities were extracted from all image pairs with GIV, filtering of the velocity data based on pixel ori-

entation, dictated by the angular direction of the glacier flow, was undertaken to exclude cells with an orientation value outside of the range of 165°–300° relative to North. This helps filter out potentially erroneous velocities resulting from false matches. The range of flow direction values accounts for ~45° of variability relative to the orientation of Airdrop's centreline in a downstream direction. The raster calculator in ArcGIS was used to exclude flow direction cells outside of the specified range. The velocity map was then clipped to the extent of the filtered flow direction map. The per-cell median value of all velocity rasters derived from Landsat 1–3 imagery was then calculated using the Cell Statistics tool in ArcGIS to produce a single velocity map for 1972–1981. This velocity stack provides a near-complete coverage of the glacier surface, as automated velocity mapping with the coarse resolution of early Landsat satellites often results in poor coverage and noisy results from individual scene pairs.

3.2.2. GAMMA InSAR

Interferometric SAR (InSAR) processing of ERS-1/2 data with GAMMA software was used to derive velocities for 1992 and 1997 at a time when optical satellite imagery was sparse at high latitudes. The ERS-1/2 scene pairs were acquired with the same orbital geometry (i.e., same path and frame) with a time separation of 30 and 35 days for 1992 and 1997, respectively, and downloaded as Level 0 (i.e., unprocessed) products from the ASF Data Search website. To compute displacements (offsets) between each pair of SAR scenes, the raw SAR data were converted to single-look complex (SLC) and multi-look intensity images in radar range-Doppler coordinates with the GAMMA Module SAR Processor.

For each scene pair in the GAMMA Interferometric SAR Processor (ISP), the first step consisted of co-registering the two images using orbit and terrain height data by resampling the second image into the geometry of the first. The offset between the two images was then computed using the orbital data and refined with a two-dimensional cross-correlation analysis. Next, the offset map was used to estimate range and azimuth displacements with a cross-correlation optimization between both scenes. Patch sizes of 160–192 range pixels by 320–384 azimuth pixels and a step size of 24 range pixels by 48 azimuth pixels were used. The displacements were thereafter converted from radar geometry to metres in ground range. To convert the displacements from SAR range/Doppler coordinates into UTM map projection coordinates, a lookup table was created from the Copernicus DEM and was applied to add the georeferencing information to the centre of every matching window used to calculate the displacements. The total displacement values were computed from:

$$\text{Total displacement} = \sqrt{(\text{range displacement}^2) + (\text{azimuth displacement}^2)} \quad (2)$$

3.2.3. NASA ITS_LIVE

NASA's Inter-mission Time Series of Land Ice Velocity and Elevation (ITS_LIVE) dataset (https://its-live.jpl.nasa.gov/; Gardner et al. 2022) was used to acquire all surface velocities of Airdrop Glacier since 1999. The NASA Jet Propulsion Laboratory derived these data predominantly from Landsat 4, 5, 7, and 8 imagery using the autonomous Repeat Image Feature Tracking (auto-RIFT v0.1) processing scheme (Gardner et al. 2018). The data are available either as individual image-pair velocities with a time separation of 6 to 546 days or as monthly or annual velocity mosaics created from the compilation of all scene-pair velocities. They have a spatial resolution of either 120 m or 240 m.

The 2000–2018 ITS_LIVE annual mean surface velocity composites for Arctic Canada North were clipped to Axel Heiberg Island. Scene-pair velocities were also acquired to fill in data gaps because some years between 2000 and 2008 had limited coverage of Airdrop Glacier. In addition, image-pair velocities were used for 2019–2021 since version 1 of the annual mosaics does not cover those years. Some years, such as 2019–2021, had a few thousand available scene-pair velocities and, therefore, had to be filtered by setting a minimum time separation between the two scenes of >60 days and/or a minimum coverage (i.e., the percentage of possible glacier pixels that have reported velocities) of 10%–90% based on the amount of data available for a specific year. After downloading all the image-pair data, the datasets with the best coverage of Airdrop Glacier (i.e., preferably with full coverage of the glacier surface and with little missing data) and the smallest errors, ranging from 4 to 7 m a^{-1}, were kept.

The GeoTIFF velocity files, along with all other rasters used in this study, were projected to NAD 1983 Zone 15 N and standardized to annual values. The errors (uncertainties) for the GIV, GAMMA, and NASA ITS_LIVE scene-pair data were estimated by quantifying the median and standard deviation (SD) of the velocity over non-glacierized terrain (i.e., bedrock) surrounding Airdrop Glacier (Table 2). Due to the presence of outliers in the data, the median value was used rather than the mean to provide a more accurate measure of central tendency. ITS_LIVE velocity error products (v_err) for the annual mosaics for 2007–2018 were downloaded, and the median and SD error values over Airdrop Glacier were computed for each year, which ranged from a median of 0.2–3.5 m a^{-1} and SD of 0.1–32 m a^{-1}. The velocity errors of the ITS_LIVE annual mosaics represent the residual sum of squares of the standard error in velocities relative to a stable surface and may be unrealistically low (http://its-live-data.jpl.nasa.gov.s3.amazonaws.com/documentation/ITS_LIVE-Regional-Glacier-and-Ice-Sheet-Surface-Velocities.pdf provides a more detailed description of how the errors were quantified).

3.3. Surface elevation

DEMs were derived for the years 1977 and 2001–2021 to measure temporal variations in surface elevation to quantify how the glacier geometry changed over the study period and whether these changes exhibit patterns indicative of surging behaviour, such as a clear redistribution of mass from an upper, reservoir zone to a lower, receiving zone (e.g., Dolgoushin and Osipova 1975).

3.3.1. sPyMicMac

A DEM was generated from a pair of stereo KH-9 Hexagon declassified images (DZB1213-500054L001001 and DZB1213-500054L002001) from 13 July 1977, enabling the surface elevation change record of Airdrop Glacier to be extended prior to the year 2000. The processing was done using sPyMicMac (https://spymicmac.readthedocs.io; McNabb et al. 2020), a set of Python tools for processing historical aerial photos and spy satellite imagery using MicMac (Rupnik et al. 2017). Before going through the general workflow, the KH-9 images need to be processed, which includes resampling, removal of Réseau marks (i.e., crosses on the photograph used as reference points to enable the correction of distortions caused by processing and handling of the film), image joining, and contrast enhancement (e.g., Maurer and Rupper 2015). Distortions in the film, caused by storage and other conditions, were rectified by resampling the images based on the locations of Réseau marks, which were automatically detected and removed by sPyMicMac. USGS scans each KH-9 image in two halves due to the large size of the film (~9″×18″), leaving a small amount of overlap that sPyMicMac uses to join the two halves together. Next, the two joined images were processed with a median filter to reduce noise by returning the median value within a kernel size of 3×3 pixels, followed by the application of a contrast stretch and a gamma adjustment to enhance the initially low contrast of both KH-9 images.

Once the pre-processing of the images was complete, the first step of the general workflow consisted of computing tie points by matching all pairs of images. Afterwards, the relative orientation of each image was determined using a basic radial distortion model and a fixed focal length. Using the orientation files created from this process, relative orthoimages and DEM were generated, and a relative orthomosaic was created from the individual orthoimages. Georeferencing the relative DEM and orthomosaic to absolute space was completed automatically with sPyMicMac by finding control points using a 2020 Sentinel-2 mosaic as the reference orthoimage, the ASTER GDEM (Global Digital Elevation Model) as the reference DEM, image footprints gathered from USGS, as well as a modified version of the Randolph Glacier Inventory (RGI) 6.0 outlines (Pfeffer et al. 2014; RGI Consortium 2017) as an exclusion mask to avoid searching for matches over glaciers or the ocean/sea ice. The control points that were computed and the folder containing the absolute orientation files were then used to compute the absolute (i.e., georeferenced) orthomosaic and DEM. A more detailed description of each step of sPyMicMac's workflow can be found at https://spymicmac.readthedocs.io/en/latest/tutorials/index.html.

3.3.2. MMASTER

MicMac ASTER (MMASTER; Girod et al. 2017) was used to derive DEMs from stereo ASTER imagery for the period 2000–2021. ASTER imagery has previously been used to produce the ASTER global digital elevation model (GDEM), but this is a blended product, meaning that the dates of individual elevations are unknown. In addition, noise is present in the satellite data in the form of "jitter" (i.e., uncorrected errors in the imagery geometry due to sensor motion), which can result in anomalies and artifacts (Girod et al. 2017). The MMASTER software package was therefore produced by Girod et al. (2017) with the goal of computing DEMs from ASTER stereo imagery that has less overall noise and fewer unmatched areas in comparison to the ASTER GDEM and NASA's AST14DMO product. The resulting DEMs have a horizontal resolution of 30 m and a vertical uncertainty of 10 m or better (Girod et al. 2017).

Using a cloud filter to exclude scenes with a cloud cover greater than 80%, a total of 816 L1A ASTER scenes (i.e., reconstructed unprocessed instrument data) were downloaded over Airdrop Glacier and its surrounding area from NASA's Earthdata Search portal. DEMs from the raw L1A raster data products were generated with batch processing of the MMASTER workflow. Running MMASTER is a computationally intensive process, so batch processing was conducted on the Cedar supercomputer from Compute Canada (https://docs.alliancecan.ca/wiki/Cedar/en). A visual inspection of the DEMs was undertaken to remove those with high levels of noise due to factors such as cloud cover and those with no coverage of Airdrop Glacier. After this, a total of 23 DEMs remained for use in the elevation change analysis, with no suitable data for 2000, 2005, 2008, and 2018.

3.3.3. Co-registration and trend analysis

A DEM co-registration script from the pybob Python package (https://github.com/iamdonovan/pybob) was used to iteratively co-register the DEMs created with sPyMicMac and MMASTER. This script is based on the co-registration algorithm described by Nuth and Kääb (2011), which removes horizontal and vertical shifts between DEMs and checks for elevation-dependent and sensor-specific biases. Overlapping bedrock elevations, which were extracted by masking glacierized pixels using the RGI 6.0 glacier outlines (Pfeffer et al. 2014; RGI Consortium 2017), were used in the batch processing of the co-registration process.

The co-registered DEMs were then post-processed by spatially and temporally filtering outliers using automated models created with ModelBuilder in ArcGIS. This was done by computing the differences between each DEM and the ASTER GDEM over the entire scene (i.e., glacier and bedrock) and by excluding pixels with a difference value greater than a certain threshold. An appropriate threshold value that would allow the differentiation of real elevation changes on the glacier surface from noise due to cloud cover or other biases was determined for each 5-year period from 2001 to 2021 by visually analyzing the elevation difference maps. Large elevation changes were consistently most notable at the terminus region of Airdrop Glacier, so second-order spatial filtering was undertaken to use a smaller threshold for the remainder of the glacier surface while keeping the original threshold value for the terminus region. Threshold values in metres of elevation difference were 85, 100, 110, and 110 for the terminus area and 40, 30, 35, and 35 for the remainder of the glacier

Fig. 2. Evolution of the terminus position of Airdrop Glacier from 1959 to 2021. The colour palette ranges from dark blue (earliest) to light blue (latest), while certain years are annotated, and their respective terminus lines are thicker to help with visual interpretation. The inset graph shows the cumulative terminus advance from 1959 to 2021 based on the results from Table 3. Base image: Landsat 8, 7 August 2020.

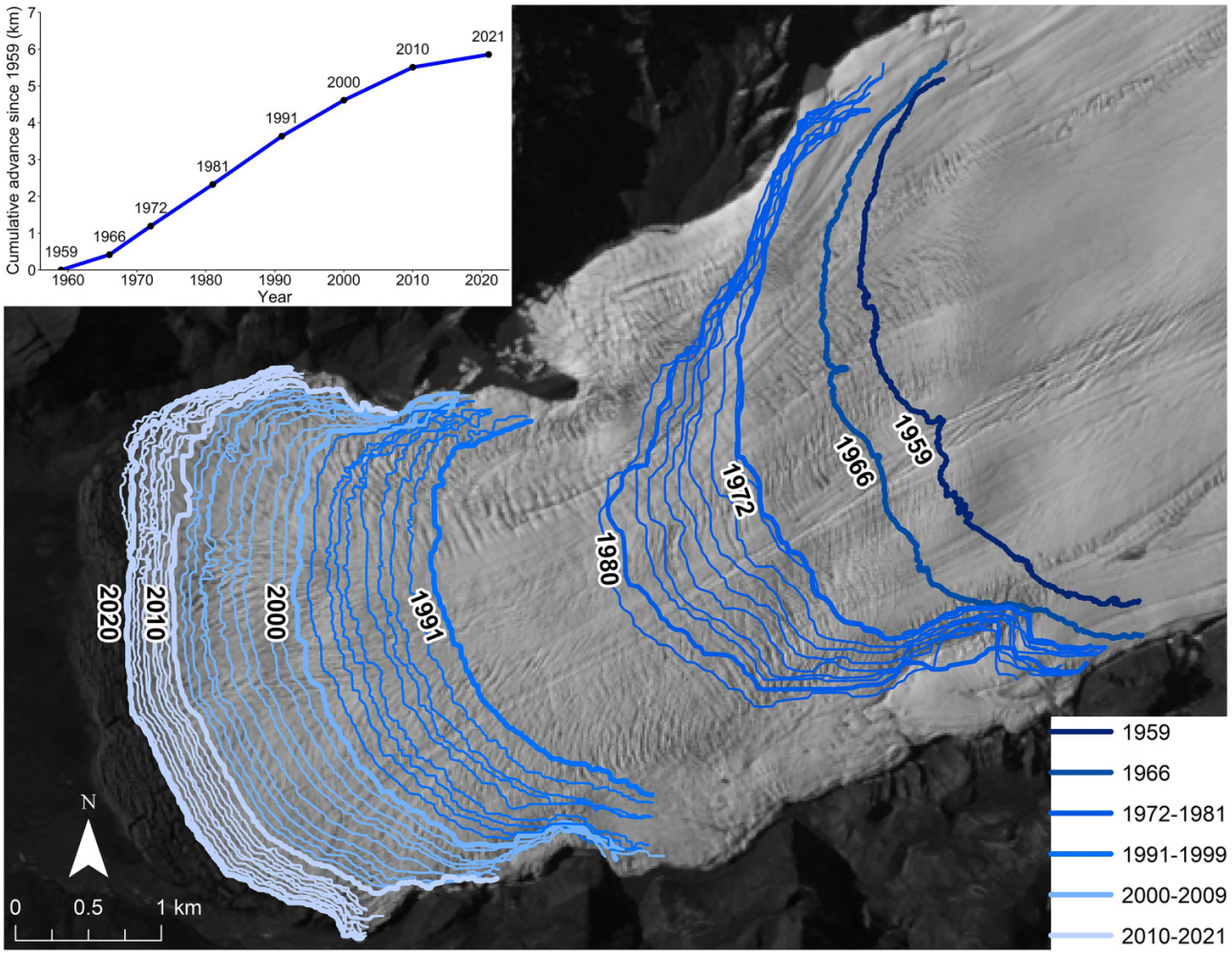

for 2001–2006, 2006–2011, 2011–2016, and 2016–2021, respectively.

Subsequently, trends in elevation changes for Airdrop Glacier were computed using the make_stack.py script from the pygeotools Python package (https://github.com/dshean/pygeotools) for the for 5-year periods 2001–2006, 2006–2011, 2011–2016, 2016–2021, as well as for 2001–2011, 2011–2021, and 2001–2021. The make_stack.py script uses a raster time series object (i.e., a stack of input rasters) from which a linear regression is calculated to compute a variety of statistics from the input DEMs, such as the minimum, maximum, mean, and trend value on a per-pixel basis. Differencing and computing trends from multiple DEMs in this way typically results in lower errors than differencing just one DEM from another. Since no other elevation datasets were available between the 1977 KH-9 DEM and the ASTER DEMs, the two DEMs were differenced, and the resulting elevation changes between 1977 and 2001 were standardized to annual values. The median elevation change trend value for 1977–2001 and 2001–2021 was computed for each 10 m elevation contour (hypsometric band) across the glacier surface, based on the mean 2001–2021 elevation values. The errors for the glacier surface elevation change trends were quantified by calculating the median absolute value over stable (i.e., non-glacierized) terrain.

4. Results

4.1. Terminus position

The terminus of Airdrop Glacier advanced ~6 km from 1959 to 2021 (Fig. 2). Most years with available imagery show an advance outside of the terminus delineation uncertainty of two pixels (~10–120 m), indicating that the glacier experienced a continuous advance over the last ~70 years. Despite this large advance, Airdrop has remained land-terminating throughout the study period, and its terminus is currently (in 2021) located ~4.5–5 km east of the ocean. Although there is no evidence of an interruption during the advance over the study period, it occurred at varying rates. From 1950 to 1959, the terminus appears to have slightly advanced, al-

Table 3. Total centreline advance and mean annual advance rates of Airdrop Glacier's terminus as well as the associated uncertainty for different periods from 1959 to 2021.

Time period	Total advance (m)	Mean advance rate (m a^{-1})	Uncertainty (m a^{-1})
1959–1966	412.9	59	8.2
1966–1972	777.6	129.6	17.6
1972–1981	1132.3	125.8	9.4
1981–1991	1311.8	131.2	6.4
1991–2000	976.3	108.5	2.6
2000–2010	897.6	89.8	2.5
2010–2021	346.1	31.5	1.9

though it is difficult to quantify this since the 1950 RCAF aerial photograph was taken in an oblique orientation pointing downglacier from Airdrop's upper half. The rate of terminus advance increased after the 1950s to average rates of >100 m a^{-1} from 1966 to 2000 and reached a peak of 131.2 ± 6.4 m a^{-1} in 1981–1991, after which it has been slowing down toward present day (Table 3; Fig. 2 inset). Airdrop's terminus advanced by a total of ~2.3 km from 1981 to 2000 but has only experienced ~1.2 km of additional advance since between 2000 and 2021. This decrease in the rate of terminus advance has been most notable from 2010 to 2021: the average advance rate over this time period (31.5 ± 1.9 m a^{-1}) was nearly three times lower than in the previous decade (89.8 ± 1.9 m a^{-1}) and more than four times lower than the peak advance rate in 1981–1991 (Table 3; Fig. 2 inset).

The shape of the terminus has altered throughout the study period as the glacier passed through a topographic constriction in the 1970s at the narrowest point of the valley, which is visible in front of the terminus in the 1959 RCAF air photo (Fig. 3*a*). The southern end of Airdrop's terminus had reached the topographic constriction by 1966, while the northern end of the terminus had reached it by 1972, restricting the transverse flow of the ice and resulting in a much narrower ice front as the ice was channelled through the constriction. Airdrop's terminus attained its largest width at less than 1 km from the ice front in 1959 (Fig. 3*a*) and at >2 km in 1977 (Fig. 3*b*). The absence of transverse ice flow is reflected by the absence of splaying crevasses along the terminus region during the 1970s (Fig. 3*b*), which later reappeared in the 1990s once the terminus started spreading out laterally again to cover a larger area as Airdrop Glacier had passed the narrowest part of the valley constriction (Fig. 3*c*). Images from 1959, 1977, 1999, and 2021 show surface features diagnostic of surging, such as heavy crevassing as well as extensive folding and looping of surface moraines (Fig. 3). Copland et al. (2003) used these observations from 1959 aerial photography and a 1999 Landsat 7 image to classify Airdrop as a "confirmed" surge-type glacier.

4.2. Velocity patterns

Ice surface velocities derived from Landsat 1–8 optical satellite imagery and ERS-1/2 SAR data show that Airdrop Glacier has not undergone any rapid variations in flow speed since the 1970s. Instead, the glacier maintained a relatively fast centreline flow rate of over 100 m a^{-1} for most of the study period, reaching nearly 200 m a^{-1} in the early 2000s at around 3 km from the 2018 terminus (Fig. 4). In contrast, land-terminating glaciers in the CAA typically flow at speeds of 25 to 50 m a^{-1} across most of their length and peak at <75 m a^{-1} near the terminus (Van Wychen et al. 2014). However, Airdrop has recently experienced a notable slowdown (Fig. 4).

The glacier had a median centreline velocity of 134 ± 36.2 m a^{-1} during the period 1972–1981 over its lowermost ~10 km (Fig. 4 and Table 2). The flow rates in the 1990s were similar, with a mean centreline velocity of 153 ± 23.8 m a^{-1} in 1992 and 141 ± 14.5 m a^{-1} in 1997 within about 12.5 km of the 2018 terminus position. The velocities peaked at >150 m a^{-1} at ~8 km from the 2018 terminus in 1992 and at ~7 km in 1997 (Fig. 4). Subsequently, the scene pair velocities from 1999–2000 to 2005–2006 show that the glacier sustained a fast flow rate during the early 2000s, with median centreline speeds ranging from 150 to 163 m a^{-1} within ~1.2–6.6 km from the 2018 terminus. Airdrop's median flow rate then dropped below 136 m a^{-1} in 2007 over the same distance and has continued to decrease since, reaching a median centreline velocity of 69 m a^{-1} in 2020–2021. The most pronounced slowdown occurred over the lower parts of the glacier (Fig. 4) as median centreline velocities decreased by ~62 m a^{-1} in the lowermost 10 km from 2007 to 2020–2021 and by 22 m a^{-1} over a distance of 20–35 km from the 2018 terminus from 2008 to 2020–2021.

4.3. Elevation changes

The continuous terminus advance and high velocities have been accompanied by considerable gains in surface elevation near the terminus of Airdrop Glacier (Figs. 5 and 6). Thickening occurred within 3–9.5 km of the 2018 terminus between 13 July 1977 and 20 May 2001, at an average rate of 3.2 ± 0.7 m a^{-1} and with a maximum single-cell value of 10 ± 0.7 m a^{-1}. Airdrop thickened at a similar rate of 3.1 ± 0.3 m a^{-1}over the period 20 May 2001 to 13 August 2021, but this was limited to within ~4.5 km of the 2018 terminus and peaked at a lower single-cell value of ~7 m a^{-1} ± 0.3 (Figs. 5 and 6). In total, these changes translate to a thickening of up to 250 ± 17 m between 1977 and 2001 and 140 ± 6 m from 2001 to 2021. These large elevation changes record the forward movement of large volumes of ice as the glacier advances over previously unglaciated terrain, as well as a redistribution of mass from the upper

Fig. 3. Progression of the terminus advance of Airdrop Glacier throughout the study period and the location of surface features characteristic of surging. (*a*) Historical air photo taken on 28 July 1959 by the RCAF; (*b*) declassified KH-9 spy satellite photo from 13 July 1977 (note that the white region in front of the terminus is from aufeis, rather than glacier ice); (*c*) Landsat 7 image from 25 July 1999; (*d*) Landsat 8 scene from 15 August 2021. Each image shows the presence of ice-surface features indicative of possible surge activity, such as looped moraines and moderately heavy crevassing. The location of a topographic constriction in the valley in which the glacier flows are indicated by white arrows in front of the 1959 terminus, and some examples of looped moraines (red arrows), extensive surface folding (orange arrows), and heavy crevassing (blue arrows) are shown in the images.

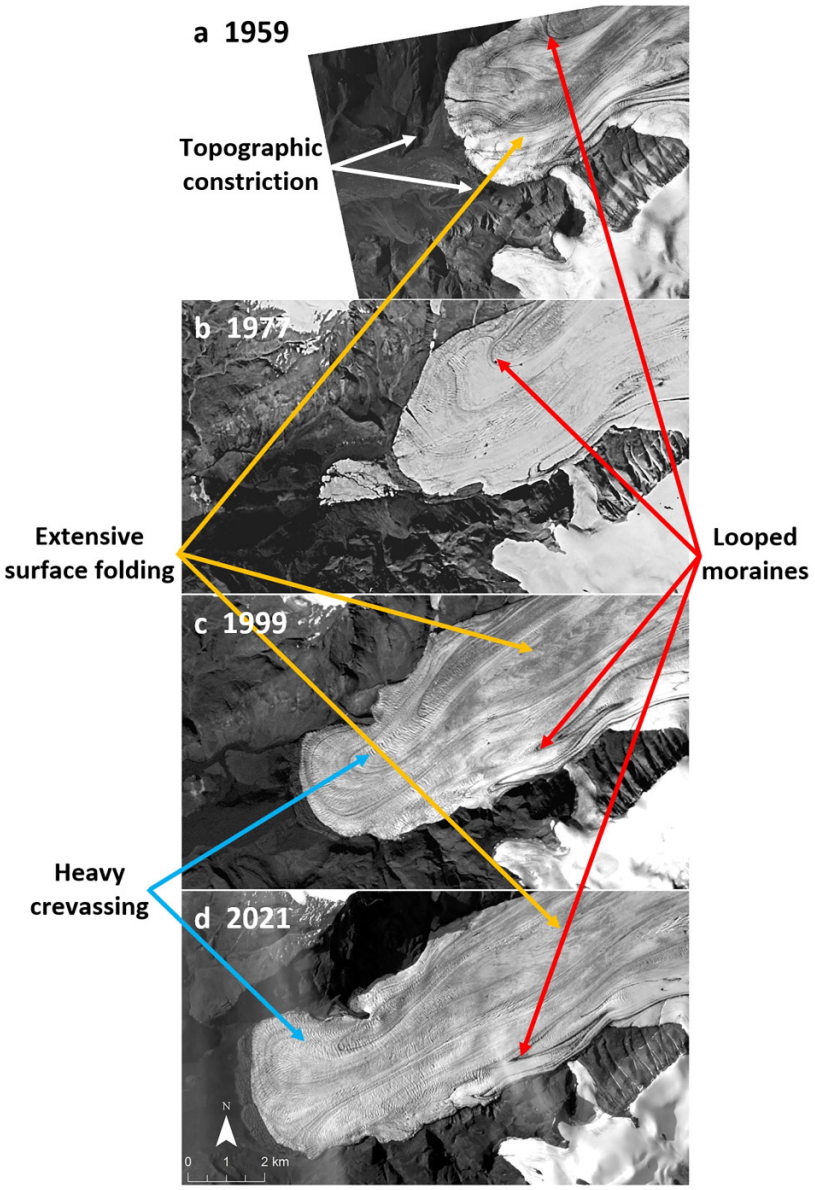

parts to the lower parts of Airdrop Glacier. Although no elevation data are available prior to 1977, we infer that a similar pattern occurred from 1950–1977 since the glacier was also advancing during that period.

The remainder of the glacier encountered thinning at an average rate of -1.7 ± 0.7 m a^{-1} across the glacier's 10 m elevation bands upstream of 9.6 km from the 2018 terminus for 1977–2001 and 0.5 ± 0.3 m a^{-1} upstream of 4.4 km from the 2018 terminus for 2001–2021 (Fig. 6). Large spatial variability is present in the 1977–2001 elevation difference results in the accumulation area of Airdrop Glacier (Fig. 5*a*), which could be the result of feature matching issues in the KH-9 imagery in these high elevation and highly glaciated areas. Median errors over nunataks in this region are ~1.4 m a^{-1}. The elevation trends computed for each 5-year period from 2001 to 2021 reveal constant thickening near the terminus across the glacier's elevation bands at median rates of up to $\sim 14.6 \pm 1.8$ m a^{-1} in 2001–2006, $\sim 10.3 \pm 1.7$ m a^{-1} in 2006–2011, $\sim 6.4 \pm 2.6$ m a^{-1} in 2011–2016, and $\sim 2.1 \pm 2$ m a^{-1} in 2016–2021. These results show a substantial decrease in

Fig. 4. Centreline surface velocities from 1972 to 2021 for Airdrop Glacier. Velocities from 1972 to 1981 represent the per-cell median of several annually separated early Landsat velocity scenes derived from feature tracking. The velocity profiles prior to 1999 were extracted from Landsat 1–3, ERS-1/2, and NASA ITS_LIVE (Gardner et al. 2018, 2022) scene pairs, while all profiles since 1999 were derived from NASA ITS_LIVE scene pairs or annual mosaics. The inset shows the temporal evolution of the median centreline velocity from 1999–2000 to 2020–2021 over the lower part of the glacier (~1.7–6.6 km from the 2018 terminus position), highlighting the significant decrease in the flow rate of Airdrop Glacier from the mid-2000s to 2020–2021.

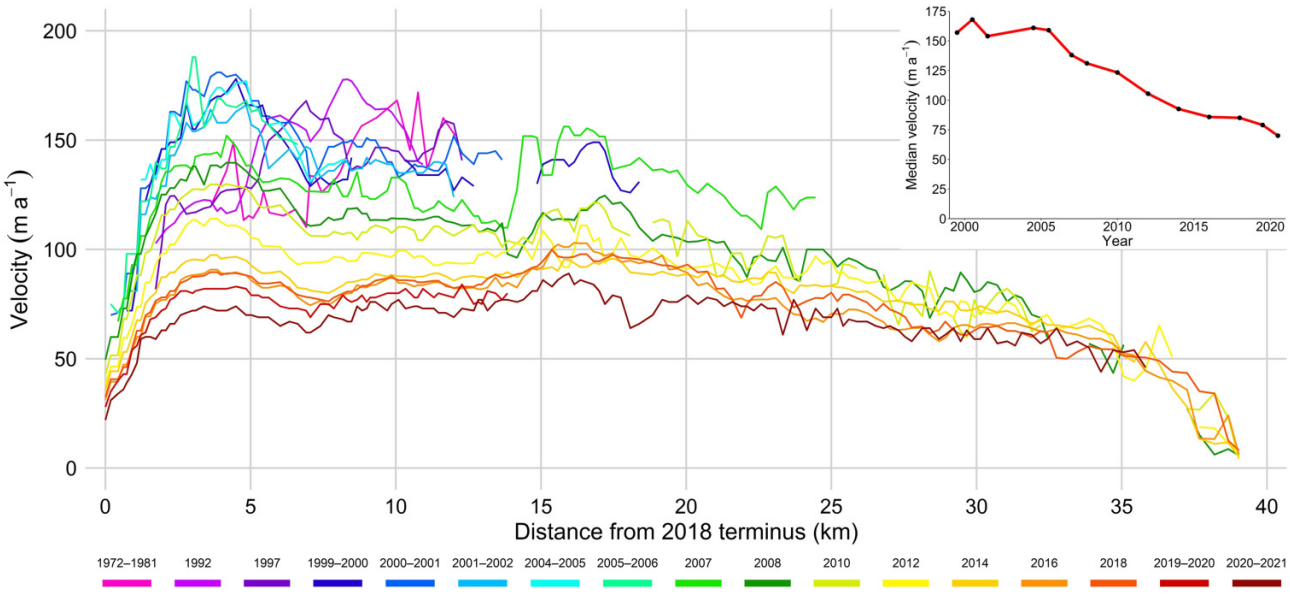

the magnitude of the surface elevation changes that have occurred within Airdrop Glacier's terminus region since the beginning of the 21st century. This reduction in rates of thickening coincides with an overall acceleration of mass loss for glaciers worldwide (Hugonnet et al. 2021), but is likely also the product of decreasing flow rates at Airdrop Glacier over this period.

5. Discussion

Glaciers typically experience sustained changes in their terminus position as a response to either external forcing or the alteration of internal conditions, but can sometimes react to a combination of the two (e.g., Dunse et al. 2015; Sevestre et al. 2018; Benn et al. 2019*b*; Haga et al. 2020). The predominant external forcing is climate since temperature and precipitation are the main controls on regional mass balance conditions (e.g., Noël et al. 2018), which, in turn, dictate whether a glacier is losing mass over time, making it susceptible to terminus retreat, or gaining mass and thus likely advancing. Internal ice flow instabilities, namely glacier surging, occur when a long period of slow flow below the glacier's balance velocity is interrupted by a large and sudden increase in flow, typically by one or two orders of magnitude (Meier and Post 2011). A marked advance of the terminus and a rapid redistribution of mass down the glacier typically follow this large acceleration, causing significant elevation changes along the glacier surface. To assess the likely cause of the long-term advance of Airdrop Glacier, we therefore consider whether changes in mass balance or surging can explain the observed changes of the glacier over the past ~70 years and then compare the dynamics of Airdrop Glacier to other surge-type glaciers on Axel Heiberg Island.

5.1. Mass balance

In situ mass balance measurements in the Canadian High Arctic have been almost continuously negative since they began in 1959 (Koerner 2005; Gardner et al. 2011; Thomson et al. 2017), and recent studies have shown that the rate of mass loss has increased throughout the 21st century (Gardner et al. 2011; Lenaerts et al. 2013; Millan et al. 2017; Mortimer et al. 2018; Noël et al. 2018; Ciracì et al. 2020). For example, long-term in situ mass balance measurements from White Glacier, located ~60 km south of Airdrop Glacier, have shown a negative glaciological balance of –213 ± 28 mm w.e. a^{-1} and a geodetic balance of –178 ± 16 mm w.e. a^{-1} for 1960–2014 (Thomson et al. 2017). Noël et al. (2018) used the regional climate model RACMO2.3 to reconstruct the daily surface mass balance (SMB) of glaciers in the CAA for the period 1958–2015. Their findings show that the northern CAA (NCAA; Ellesmere, Devon, Axel Heiberg, and Meighen Islands) was subject to a negative mass budget of 11.9 ± 11.5 Gt a^{-1} for 1958–1995, and that the rate of mass loss more than doubled to a total of 28.2 ± 11.5 Gt a^{-1} for 1996–2015 (Noël et al. 2018). A more recent study by Ciracì et al. (2020) that used the Gravitational Recovery and Climate Experiment (GRACE) and GRACE Follow-On data from April 2002 to September 2019 quantified an even higher mass loss of 41.2 ± 7 Gt a^{-1} for the NCAA. The recent increase in mass loss in the CAA is linked to an increase in runoff and longer melt seasons induced by rising summer air temperatures (Gardner et al. 2011; Lenaerts et al. 2013; Mortimer et al. 2018; Ciracì et al. 2020). Surface melt,

Fig. 5. Airdrop Glacier surface elevation change trends for the periods (*a*) 1977–2001 and (*b*) 2001–2021. The 1977–2001 trends were computed by subtracting the 1977 DEM from the 2001 DEM, while the 2001–2021 trends were derived from multiple DEMs using the make_stack.py script from the pygeotools Python package (https://github.com/dshean/pygeotools). Cells with a value within the range of −0.5 to 0.5 m a^{-1} are excluded for both periods, representing the average of the 1977–2001 (−0.7 to 0.7 m a^{-1}) and 2001–2021 (0.3–0.3 m a^{-1}) errors. Base image: Landsat 8 composite image.

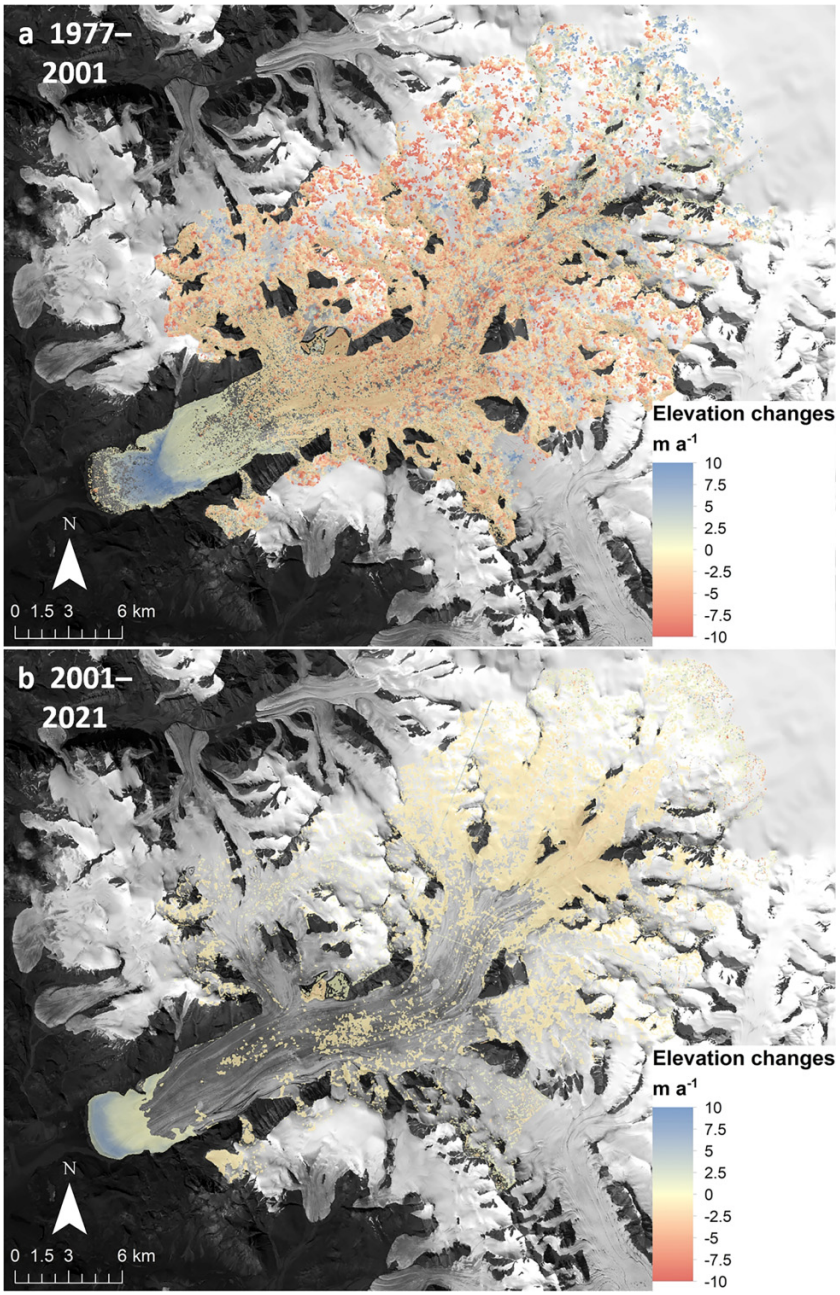

which increases runoff, accounted for ~90% of the mass loss in the Queen Elizabeth Islands from 2005 to 2014, while the remaining ~10% was from ice discharge (Van Wychen et al. 2014). In comparison, ice discharge made up 52% of the total mass loss from 1991 to 2002, when surface melt rates were lower (Millan et al. 2017).

This sustained mass loss has resulted in the retreat, slowdown, and thinning of most glaciers in the CAA, most notably land-terminating glaciers (Thomson et al. 2011; Schaffer et al. 2017; Strozzi et al. 2017; Thomson and Copland 2017; Thomson et al. 2017; Mortimer et al. 2018). In situ differential GPS measurements on White Glacier show a 31%–38% slowdown at lower elevations (400 and 600 m a.s.l.) between 1960–1970 and 2012–2016, but no detectable changes in annual velocities at higher elevations (~850 m a.s.l.; Thomson and Copland 2017). The observed slowdown has been associated with a decrease in internal ice deformation as a result of glacier thinning and a reduction in basal motion likely due to increased hydraulic efficiency (Flowers 2015; Thomson and Copland 2017), reducing basal water pressure and, in

Fig. 6. Median glacier surface elevation change trends observed in each 10 m hypsometric band for the periods 1977–2001 (blue) and 2001–2021 (red). The 1977–2001 trends were calculated from the differencing of the 1977 and 2001 DEMs, while the 2001–2021 trends were derived from multiple DEMs using the make_stack.py script from Shean et al. (2016).

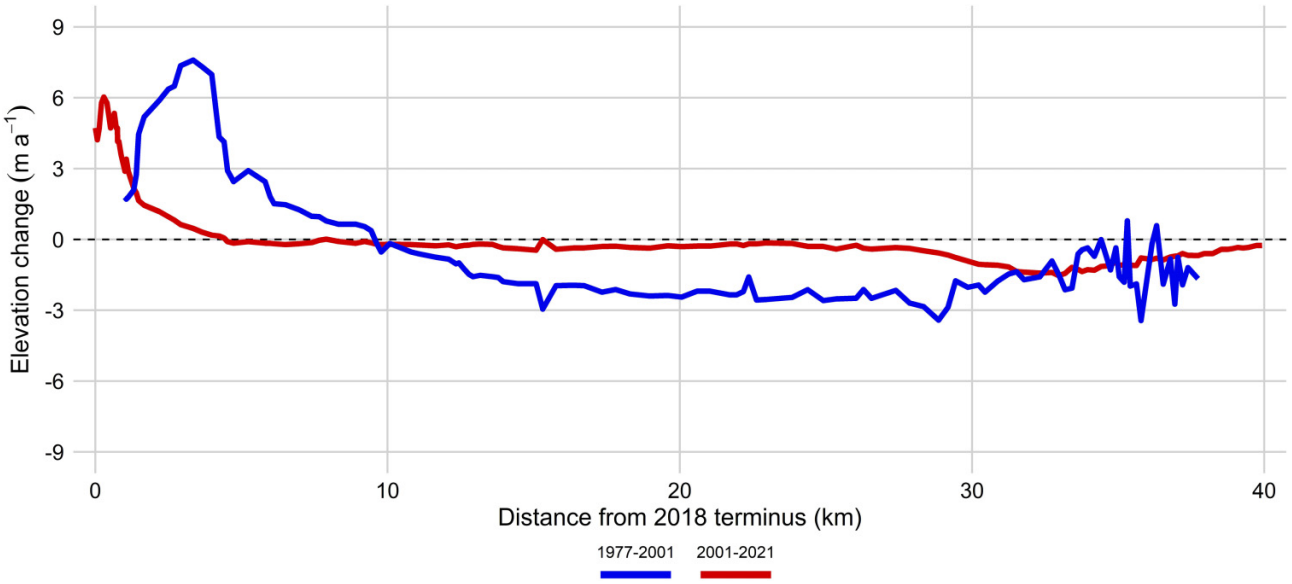

turn, increasing friction at the glacier bed (Iken and Bindschadler 1986). SMB data compiled by Noël et al. (2018) reveal median ice equivalent losses over Airdrop of 0.28 ± 0.18 m a^{-1} (240 mm w.e. a^{-1}) for 1958–1995 and 0.73 ± 0.18 m a^{-1} (611 mm w.e. a^{-1}) for 1996–2015 (https://doi.pangaea.de/10.1594/PANGAEA.881315), assuming an ice density of 850 ± 60 kg m^{-3} (Huss 2013). However, annual SMB measurements from nearby White Glacier show a median value close to zero (+0.08 mm w.e. a^{-1}) from 1964 to 1976 (Thomson et al. 2017). Although this coincides with an apparent acceleration in the advance rate of Airdrop Glacier, a near-neutral mass balance in this region over a 12-year period is likely not sufficient to drive such a sustained advance. Therefore, the overall negative mass balance regime in the region since at least 1958 cannot explain the observed behaviour of Airdrop Glacier over the study period.

Studies have used numerical modelling to find relationships between glacier size, ice thickness, surface slope, elevation range, ablation rate, mass balance gradient, and the time it takes for an ice mass to respond to an external forcing, such as changes in climatic conditions (Jóhannesson et al. 1989; Bahr et al. 1998; Pfeffer et al. 1998; Raper and Braithwaite 2009; Zekollari et al. 2020). Raper and Braithwaite (2009) showed that in cold climates, glacier volume response time can increase with glacier area, with Axel Heiberg Island having the lowest mass balance sensitivity (i.e., temperature sensitivity of mass balance) of the seven regions that were studied. Their results also show that the response time of large glaciers on Axel Heiberg Island can be hundreds of years longer than that of small ice masses (Raper and Braithwaite 2009). This is supported by the area change observations on Axel Heiberg by Thomson et al. (2011), who found that independent ice masses smaller than 25 km^2 experienced significant retreat or disappeared entirely between 1959 and 2000, while the considerably larger outlet glaciers from Müller and Steacie Ice Caps either advanced or retreated slightly. Some of the observed advance has been attributed to surge activity (Thomson et al. 2011). The island lost <1% (15.92 km^2) of its ice coverage during that period, although 90% of ice masses smaller than 0.2 km^2 completely disappeared. Despite the overall mass loss, eight large hydrological basins mostly centred around Müller Ice Cap exhibited, on average, a ~5% increase in ice area, and the greatest growth of 77.81 km^2 occurred in the Iceberg Bay basin (Thomson et al. 2011).

Variations in response time can also be illustrated by comparing the recent terminus changes of the White, Thompson, and Good Friday glaciers (Fig. 1). White Glacier has narrowed and retreated by approximately 250 m between 1958 and 1995 (Cogley et al. 1996*b*), and its area has decreased from 41.07 km^2 to 38.54 km^2 from 1960 to 2014 (Thomson and Copland 2016; Thomson et al. 2017). Conversely, the terminus of Thompson Glacier, adjacent to White Glacier, advanced by about 950 m over the period 1958–1995 and has only started retreating sometime in the 2000s (Cogley et al. 1996*b*; Cogley et al. 2011). A possible explanation for the contrasting behaviour of these two neighbouring glaciers is that Thompson Glacier, being an order of magnitude larger than White Glacier (384 km^2 versus 39.4 km^2), has a longer response time (Cogley et al. 2011). Therefore, the prolonged advance of Thompson Glacier in comparison to White Glacier could have been the result of a delayed response to the positive mass balance conditions that prevailed during the Little Ice Age (LIA) cooling (Cogley et al. 2011), which took place from ~1275–1375 to 1850–1900 in the Canadian Arctic (Moore et al. 2001; Miller et al. 2012; Barry and Hall-McKim 2019; Kochtitzky et al. 2023).

The uninterrupted terminus advance of Good Friday Glacier since the late 1940s has also been interpreted by

Medrzycka et al. (2019) to be potentially related to the positive mass balance conditions of the LIA, suggesting that its advance could perhaps be explained as a continuing response to this environmental forcing due to its large total basin size of ~800 km^2 and hence its longer response time than both White and Thompson glaciers (Raper and Braithwaite 2009). Considering Airdrop's similar total basin size (~600 km^2) and behaviour, we propose that a delayed response to the LIA is one of the likely explanations for the glacier's advance over the last seven decades.

5.2. Glacier surging

A dynamic instability, particularly glacier surging, offers another potential explanation for the observed dynamics of Airdrop Glacier. Surges are thought to arise when balances in both enthalpy and mass flux are not met, preventing the glacier from remaining in a stable steady state by periodically increasing mass flux to evacuate the buildup of excess enthalpy at the glacier bed (Sevestre and Benn 2015; Benn et al. 2019*a*). Enthalpy production is driven predominantly by internal factors, including the conduction of heat from the glacier bed to the atmosphere and the runoff of basal meltwater, but can also be affected by external factors, such as the intrusion of summer surface melt to the glacier bed through crevasses and moulins, causing a hydro-thermodynamic feedback (Dunse et al. 2015; Benn et al. 2019*a*).

In cold, dry environments such as the CAA, where glacier velocities are typically low and thus basal enthalpy production is minimal, surge-type glaciers tend to be large and thick. This is because larger glaciers have higher basal enthalpy production from higher balance velocities, coupled with less efficient enthalpy dissipation from conductive heat losses to the atmosphere due to the greater ice thickness, making them less likely to find a balance between enthalpy production and enthalpy loss (Sevestre and Benn 2015). In fact, the largest surge-type glaciers of all surge clusters worldwide are found in the Canadian Arctic, with an average area of 627 km^2 (Sevestre and Benn 2015). Copland et al. (2003) and Sevestre and Benn (2015) have identified a total of 51 and 54 surge-type glaciers in the Canadian Arctic with remote sensing and modelling, respectively, but more recent studies have found additional surge-type glaciers (e.g., Van Wychen et al. 2016, 2022).

Several glacier surface features, such as looped medial moraines, intense folding visible at the surface, extensive crevassing, and a heavily broken-up surface, can be detected using aerial photography or satellite imagery and can provide an indication of possible surging activity (Copland et al. 2003). Copland et al. (2003) identified Airdrop Glacier as a surge-type glacier and inferred that the glacier was actively surging in 1999 based on the presence of heavy crevassing, surface folding and looping, and the ~4.5 km terminus advance that occurred between 1959 and 1999. We have observed the same surface features diagnostic of surging throughout the entire study period (Fig. 3), which can be interpreted as signs of unstable flow, but do not in themselves provide sufficient evidence of past surging activity. In fact, any periodic speedup of a glacier that is not related to surging, such as a response to a positive change in mass balance, can produce these surface characteristics. Alternatively, the looped moraines may have formed as Airdrop Glacier advanced into previously unglaciated terrain and entrained the terminal moraines of smaller glaciers flowing perpendicular to Airdrop and reaching the sides of the main valley floor. Other characteristics suggestive of a surge include high surface velocities over nearly the entire length of the glacier, thickening in the lowermost ~4–8 km of Airdrop Glacier and thinning over the rest of its surface, as well as a recent slowdown that was interpreted as a long transition into quiescence, occurring over a period of a decade or more (Van Wychen et al. 2021). However, thinning at higher elevations remained relatively minimal (Figs. 5–7), namely from 2001 to 2021, in comparison to what would be expected of a glacier that is undergoing a classical surge within the same region (e.g., Lauzon et al. 2023).

Previous studies have proposed that Airdrop Glacier began surging sometime between 1975 and 1999 (Thomson et al. 2011) and that it was still actively surging in the mid-2000s before it started slowing down (Van Wychen et al. 2021). Our results suggest that surge initiation occurred prior to 1975 and could have instead taken place in the late 1950s or early 1960s as the glacier's terminus advance rate notably increased following its seemingly minimal 1950–1959 advance. Nevertheless, the scarcity of imagery prior to 1972 impedes our ability to precisely determine when the glacier would have started surging, and the earliest available aerial photograph from 1950 was oblique, making it challenging to accurately determine its position relative to the next photo in 1959. In addition, Airdrop's flow rate for 1972–2021 has varied little other than the constant slowdown that has occurred since the mid 2000s (Fig. 4), and surface elevation change patterns show a long-term pattern of thickening near the terminus and thinning across the rest of the glacier since at least 1977 (Figs. 5 and 6). Although surge cycles are hypothesized to last up to 500 years in Svalbard (Dowdeswell et al. 1991), the longest active phase ever thought to be recorded of 50+ years has been observed on Split Lake Glacier in the Canadian Arctic (Van Wychen et al. 2022). Therefore, if Airdrop Glacier is indeed surging and was already surging in the 1950s, it would have a similar, or even greater, active phase length of more than 70 years.

5.3. Distinguishing between surging and advancing glaciers

A case study in the eastern Karakoram by Lv et al. (2020) used optical satellite imagery to compare the spatial and temporal changes of a glacier that was surging to an adjacent glacier that was advancing. Their results showed three major differences between the two types: (1) the advancing glacier moved forward at a steady rate, while the surging glacier advanced dramatically upon surge initiation; (2) the surging glacier underwent significant fluctuations in surface velocity throughout the active phase, while the advancing glacier flowed at a steady rate throughout the study period; and (3) surface elevation changes indicate a redistribution of mass from a thinning reservoir zone to a thickening receiving zone

Fig. 7. Mean surface mass balance (SMB; derived from Noël et al. (2018)), geodetic mass balance (GMB; derived from DEM differencing), and dynamic mass balance (DMB; derived by subtracting SMB from GMB) over the trunk of Airdrop Glacier at 1 km spatial resolution, computed across 50 m hypsometric bands for (*a*) 1977–2001 and (*b*) 2001–2021.

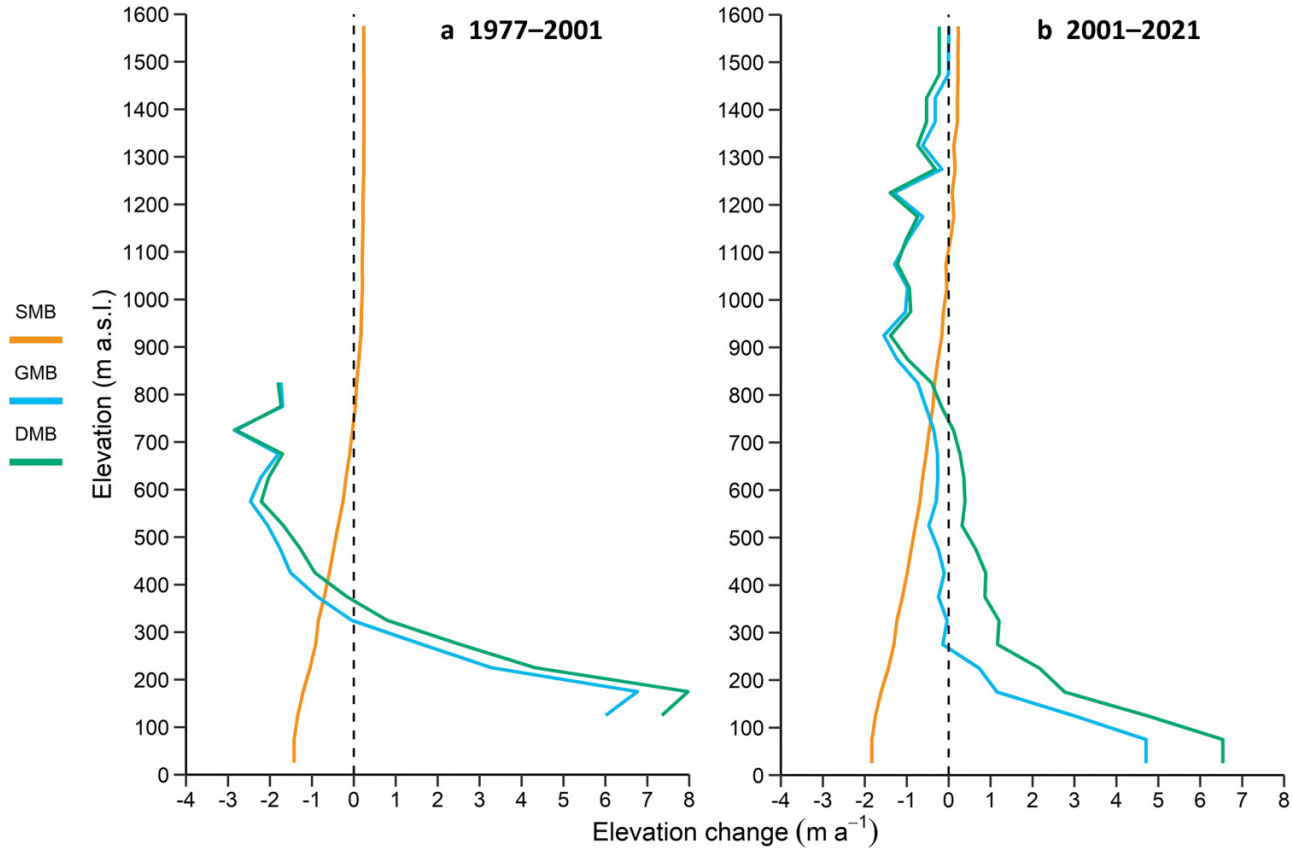

for the surging glacier, but the advancing glacier appears to only have thickened over its terminus part, without any other significant elevation changes over the rest of the glacier surface (Lv et al. 2020). Unlike Airdrop Glacier, which has had an overall negative mass balance for several decades (Koerner 2005; Gardner et al. 2011; Lenaerts et al. 2013; Millan et al. 2017; Mortimer et al. 2018; Noël et al. 2018; Ciracì et al. 2020), the advancing glacier studied by Lv et al. (2020) had a slightly positive mass balance of 270 ± 40 mm w.e. a^{-1} from 1995 to 2019, which could explain why it had not started decelerating like Airdrop. In fact, balanced to slightly positive glacier budgets have dominated in the Karakoram over the past two decades, resulting in some glaciers advancing and encountering increases in their flow speed (e.g., Farinotti et al. 2020). This is in stark contrast to glaciers in other regions, which are retreating and slowing down, and therefore, characteristics 1 and 2 mentioned above are more specific to this region of High Mountain Asia. Regardless, our observations reveal that Airdrop Glacier has behaved most similarly to the advancing glacier described in Lv et al. (2020), as there have been no significant fluctuations in the advance and flow rates of Airdrop since at least 1959 other than the persistent slowdown that has occurred since ~2005 (Table 3 and Fig. 4), and the most prominent elevation changes for 1977–2021 occurred near the terminus (Figs 5 and 6). The main dissimilarity is that the advancing glacier in the Karakoram did not experience any thinning at higher elevations, which could again be partly due to differences in SMB conditions between the two regions or because Airdrop Glacier is undergoing dynamic instability.

The mean geodetic mass balance values of the main trunk of Airdrop Glacier for 2001–2021, computed across 50 m hypsometric bands at a resampled spatial resolution of 1 km, are highest at the current terminus position (0–50 m a.s.l.) with a value of ~4.7 m a^{-1}, decreasing in an upstream direction to its lowest value of approximately −1.5 m a^{-1} (Fig. 7*b*) at ~33 km from the 2018 terminus position (900–950 m a.s.l.). On the other hand, SMB data from Noël et al. (2018) for the period 1996–2015 show a drastically different trend of quasi-linear increase from a minimum value of approximately −2 m a^{-1} at the current terminus to a maximum value of about 0.2 m a^{-1} (Fig. 7*b*) at >40 km from the 2018 terminus (>1400 m a.s.l.). This suggests that the observed surface elevation changes during this time period cannot be attributed to SMB alone. The dynamic mass balance (DMB) of the Airdrop Glacier for 2001–2021, which was computed by subtracting the SMB from the geodetic mass balance at 1 km spatial resolution, shows a redistribution of mass downglacier from the upper part of the glacier, with thinning rates exceeding −1 m a^{-1} (Fig. 7*b*) above ~32 km from the 2018 terminus (above ~900 m a.s.l.). The dynamic mass balance of a glacier is defined as a change in glacier volume caused by a dynamic

deviation of flow rates from the balance velocity, rather than by variations in accumulation and ablation (Pfeffer 2007). The glacier surface was, according to the dynamic mass balance from 2001 to 2021, mostly subject to thickening up to ~28 km from the 2018 terminus. The magnitude of this thickening increased in a downglacier direction, with trunk-wide mean rates of >1 m a^{-1} below ~9 km from the 2018 terminus and reaching >6 m a^{-1} near the terminus (Fig. 7*b*).

The 1977–2001 elevation differencing results show trends that are broadly similar to the more recent period (2001–2021) despite the large amount of noise in the 1977 KH-9 elevation data (Fig. 5a), although the glacier appears to have experienced greater elevation changes in 1977–2001 than in 2001–2021. For instance, geodetic mass balance changes peaked at almost 7 m a^{-1} (DMB of ~8 m a^{-1}) near the terminus, became negative above 300–350 m a.s.l. (350–400 m a.s.l. for DMB), and dropped to about −1.5–3 m a^{-1} at an elevation of ~400–850 m a.s.l, or at 500–850 m a.s.l. for DMB (Fig. 7*a*). No reliable geodetic mass balance data could be computed above 850 m a.s.l. due to larger errors in these higher elevation, snow-covered areas. This suggests that a greater drawdown of mass occurred from 1977 to 2001 than from 2001 to 2021, which is consistent with the quicker rate of terminus advance and higher flow rates, on average, during the earlier period (Table 3 and Fig. 4). The geodetic and dynamic mass balance trends throughout the study period are in line with surging behaviour during the active phase, where mass is transferred downglacier from the upper reservoir zone to the lower receiving zone. However, it is unclear whether the measured drawdown in the upper region could instead be the result of the sustained high velocities over the entire glacier length if the glacier is still responding to the climatic forcing of the LIA, resulting in a high emergence velocity in the ablation area. In that case, the recent deceleration of Airdrop, which has occurred in parallel with a reduction of its advance rate and thickening rate near the terminus, would constitute a gradual transition towards the glacier's balance velocity under the current environmental conditions rather than a transition to the quiescent phase. If this slowdown persists, Airdrop Glacier could soon start retreating, akin to what has recently happened to nearby Thompson and White glaciers (Cogley et al. 1996*a*, 1996*b*, 2011; Thomson et al. 2011).

5.4. Evidence for a slow surge

If Airdrop is defined as surge-type, then its long active phase would be best fitted under the category of a slow surge (Jiskoot 2011). Unlike typical surging glaciers, which usually undergo an increase in velocity of two or three orders of magnitude (Meier and Post 2011), slowly surging glaciers have flow rates 5–10 times higher than during the quiescent phase (Jiskoot 2011). Slow surges also tend to be longer, with an active phase duration of more than 20 years, and sometimes result in no change in terminus position (Jiskoot 2011). Slowly surging glaciers have been observed in a few regions with differing climatic conditions, such as Yukon, Svalbard, and the Canadian Arctic (Frappé and Clarke 2007; Sund et al. 2009; Flowers et al. 2011; Van Wychen et al. 2022). Flow speeds during a slow surge can be much lower than during an ordinary surge, as exemplified by the ~20-year surge of Trapridge Glacier in the St. Elias Mountains, Yukon, which saw only a slight acceleration from 16 to 42 m a^{-1}, but had an identifiable downglacier-propagating surge front and experienced a 10% increase in its area during the surge (Frappé and Clarke 2007).

A recent study has provided a detailed analysis of the slow surge of the land-terminating Split Lake Glacier (437.8 km^2), on SE Ellesmere Island, which has been advancing since ~1970 at flow rates that reach >600 m a^{-1} (Van Wychen et al. 2022). Large variations in ice motion were recorded around 1970 when the glacier started surging, and between 1999 and 2002 when the glacier underwent a temporary slowdown (Van Wychen et al. 2022). In contrast, Airdrop Glacier has not experienced any rapid changes in velocity typical of surge-type glaciers since at least the 1970s, and the lack of early imagery makes it challenging to identify when surge initiation would have occurred. While thinning at higher elevations is of a lesser magnitude than what is typical of a glacier that is actively surging, particularly for 2001–2021, the measured surface elevation changes are more consistent with a slowly surging glacier, which can only be detected with high-accuracy geodetic measurements (Jiskoot 2011). In fact, a slow surge has been suggested as a possible alternate explanation for the long advance of Thompson Glacier (Fig. 1) due to the presence of large looped and folded moraines (Copland et al. 2003; Cogley et al., 2011). The long-term advance of Good Friday Glacier could also be the result of a similar phenomenon. Although the dynamics of these three glaciers closely resemble the behaviour of slowly surging glaciers, the lack of evidence in the available datasets of a clear surge initiation or of other definitive periodic oscillations in ice motion outside of the study period for any of these glaciers makes it difficult to determine whether the advance of their termini was driven by a slow surge.

5.5. Comparison to other surge-type glaciers on Axel Heiberg Island

The three glaciers on Axel Heiberg Island that were classified as surge-type by Copland et al. (2003) (Airdrop: ~600 km^2, Good Friday: ~800 km^2, and Iceberg: ~1000 km^2) were inferred to be surging in the 1990s based on the presence of large looped moraines, heavy crevassing, extensive surface folding and looping, and significant advances of ~4.5–7 km between 1959 and 1999. These glaciers alone, which constitute the island's largest outlet glaciers, added 85.45 km^2 of ice to the island's glacier inventory between 1959 and 2000 (Thomson et al. 2011).

Iceberg Glacier is the only ice mass on Axel Heiberg Island that has shown cyclic behaviour that is typical for surge-type glaciers since it has now been observed in both the active and quiescent phases of the surge cycle (Copland et al. 2003; Van Wychen et al. 2016; Medrzycka et al. 2019; Lauzon et al. 2023). The surge of Iceberg Glacier lasted from approximately 1981 to 2003, with a rapid rise in ice motion at surge initiation and velocities attaining >2000 m a^{-1} at the terminus in summer 1991, more than an order of magnitude higher than the highest velocity on record for Airdrop Glacier, and resulting

in a maximum terminus advance of more than 7 km. Surface elevation change trends reveal that the glacier gains mass in its reservoir zone and loses mass in its receiving zone during quiescence, while the opposite occurs during a surge. The major difference between the two glaciers is that Airdrop has only encountered relatively small fluctuations in its patterns and rates of terminus change, flow, and ice thickness, while Iceberg experienced dramatic changes in its dynamics over the same period as the glacier underwent an entire surge cycle. For example, Iceberg Glacier accelerated by a factor of >50 in parts of its terminus region in 1981 compared to its 1972–1980 mean velocity, while the glacier's flow rate decreased by a factor of three in less than a year in 1999/2000 as the glacier was nearing surge termination (Lauzon et al. 2023). In comparison, Airdrop Glacier experienced a less pronounced slowdown in 15 years. It is perplexing as to why two adjacent glaciers would behave in such different manners, but the fact that Iceberg Glacier is marine-terminating is an important factor to consider. The tidewater dynamics at the front of this glacier could play a role in regulating velocities since the flow of such glaciers is controlled by several additional mechanisms occurring at the ice-ocean interface (e.g., Nick et al. 2009). Subglacial topography measurements from 3D tomography radio-echo sounding data collected by NASA Operation IceBridge (https://data.cresis.ku.edu/) revealed that Iceberg Glacier was retreating into deeper water before it surged, increasing extension and, therefore, thinning rates and velocities at the glacier front until the terminus likely reached flotation (Lauzon et al. 2023). Low effective pressure at the terminus due to high basal water pressure would have enabled a much larger increase in frontal flow rates than would be typical of a land-terminating glacier, such as Airdrop.

Conversely, the overall dynamics of Good Friday Glacier resemble those of Airdrop Glacier much more than those of Iceberg Glacier, despite Good Friday Glacier being marine-terminating for most of the last 50 years (Medrzycka et al. 2019). The main difference between the two glaciers is that velocities are currently highest at the terminus of Good Friday Glacier (Medrzycka et al. 2019), while velocities at the terminus of Airdrop Glacier sharply decrease. These are typical velocity patterns for marine-terminating and land-terminating glaciers in the CAA (Van Wychen et al. 2021). Good Friday Glacier has advanced by ~9.3 km since observations began in 1948 and has maintained relatively high velocities of >100 m a^{-1} across most of its length (Medrzycka et al. 2019). Good Friday Glacier has nonetheless slowed down by ~50–100 m a^{-1} over much of its length throughout the last decade, accompanied by a considerable decrease in the rate of terminus advance in the last few years (Medrzycka et al. 2019), which is analogous to what has occurred to Airdrop Glacier over a similar period. While Medrzycka et al. (2019) also suggested surging and a delayed response to the positive mass balance regime of the LIA as plausible causes for the observed dynamics, an alternate explanation was given, stating that the glacier terminus could have experienced a single period of unstable advance resulting from perturbations in bedrock topography. The presence of a topographic high 9 km from Good Friday's 2018 terminus position has caused a localized velocity peak along with steepening and surface drop downstream from the bedrock bump as well as thickening upglacier from it (Medrzycka et al. 2019). However, this small-scale perturbation in basal topography is unlikely to account for the relatively high flow rates observed along the entire glacier length. There are no available data on Airdrop Glacier's underlying topography, so this hypothesis cannot be tested in this study.

Although the recent slowdown of both Airdrop and Good Friday has previously been interpreted as a possible gradual shift into quiescence and both glaciers have characteristic surge features (Medrzycka et al. 2019; Van Wychen et al. 2021), the lack of direct evidence of a surge initiation or surge termination, or of the propagation of a surge front, makes it difficult to assert whether the observed dynamics of Airdrop and Good Friday glaciers are influenced by surging or any other dynamic instability. The nearly simultaneous decrease in the flow rates for two similarly sized glaciers raises the alternate explanation that the glaciers could be starting to adjust to the negative mass balance conditions of the last several decades following the positive mass balance conditions of the LIA. However, an in-depth quantitative analysis of glacier response to variations in climate in this region would be needed to fully support or reject this hypothesis, which cannot be done reliably with the currently available data.

6. Conclusions

The observations in this study indicate that Airdrop Glacier has undergone a continuous advance of ~6 km since the 1950s, related to sustained high centreline velocities of >100 m a^{-1} during most of the study period. This has resulted in a drawdown of mass and pronounced thickening over the glacier's terminus region, causing surface elevation changes that are significantly different from those predicted from SMB modelling (Noël et al. 2018). These patterns markedly contrast with the dominant regional trend of glacier retreat, slowdown, and thinning over the past several decades in the CAA in response to increasingly negative mass balance conditions (Gardner et al. 2011; Thomson et al. 2011; Lenaerts et al. 2013; Millan et al. 2017; Schaffer et al. 2017; Strozzi et al. 2017; Thomson and Copland 2017; Thomson et al. 2017; Mortimer et al. 2018; Noël et al. 2018; Ciracì et al. 2020). This strongly suggests that the climatic conditions since the late 1940s are unlikely to explain the observed dynamics of Airdrop Glacier over most of the study period.

The dynamics of Airdrop Glacier, paired with the presence of surface features indicative of surging, such as heavy crevassing and extensive folding and looping of moraines, instead suggest that the large terminus advance could have resulted from a surge. The progressive slowdown of >50 m a^{-1} that has occurred over the last ~15 years could then be interpreted as the glacier transitioning to the quiescent phase of the surge cycle. If the glacier is indeed surging, the active phase that potentially spans more than seven decades and the relatively low velocities compared to other nearby surge-type glaciers (e.g., Iceberg Glacier; Lauzon et al. 2023) would be best aligned with the definition of a slow surge (Jiskoot 2011). The apparent acceleration in the rate of termi-

nus advance in the 1960s and 1970s compared to the 1950s could possibly indicate the onset of a surge, but the sparsity of imagery between 1950 and 1972 and the change in terminus width as it passed a bedrock constriction make it difficult to know precisely how and why the glacier was changing prior to the satellite era. The observed surface features, terminus advance, high ice velocities, and surface elevation change trends do not in themselves provide conclusive evidence for surging or any other dynamic instability. The lack of evidence of periodic oscillations in flow rates or any previous fast flow events prevents us from deducing that the behaviour of Airdrop Glacier over the last 70 years is cyclic in nature.

An alternate explanation for the discrepant behaviour of Airdrop Glacier compared to similar glaciers in the CAA, and with recent climatic conditions, is its long response time to external forcing. Previous studies have found a relationship between the size of a glacier and its response time (Bahr et al. 1998; Pfeffer et al. 1998; Raper and Braithwaite 2009; Zekollari et al. 2020), which is reflected on Axel Heiberg Island by the asynchronous start of terminus retreat between glaciers of different sizes following the persistent negative mass balance conditions of the last several decades (Cogley et al. 1996*a*; Cogley et al. 2011). This out-of-sync behaviour between adjacent glaciers has been interpreted as potentially linked to variations in response times to the climatic conditions of the LIA, which favour a positive mass balance regime (Cogley et al. 2011; Medrzycka et al. 2019). Considering that Thompson Glacier (384 km^2) kept advancing until the 2000s (Cogley et al. 2011), Airdrop Glacier could still be responding to the LIA cooling, taking into account its longer response time owing to its larger size (~600 km^2). Airdrop and Good Friday glaciers both experienced a decrease in their flow and advance rates over the last ~10–15 years, which could indicate that these two glaciers are starting to respond to the negative mass balance conditions that have prevailed throughout the ~70-year study period. This response to recent climatic conditions can occur whether these glaciers are surging or not, and it is thus possible that both flow instability and a delayed response to the positive mass balance conditions of the LIA could be simultaneously responsible for the abnormal behaviour exhibited by these glaciers.

Future investigations should keep track of the velocities of Airdrop Glacier to determine whether its ongoing slowdown stabilizes to the typical flow rates for land-terminating glaciers in the Canadian Arctic of 20–50 m a^{-1} along the trunk and <75 m a^{-1} near the terminus (Van Wychen et al. 2014), or drops below the glacier's balance velocity to stagnant levels (i.e., <20 m a^{-1}). Bed tomography and ice thickness measurements could also allow us to analyze the role of the bedrock topography in driving the glacier's dynamics. Testing the enthalpy balance theory of surging proposed by Benn et al. (2019*a*, 2019*b*) could verify whether their model can predict the glacier's observed sequence of events and could provide insights into why the surge dynamics of adjacent Iceberg Glacier differ from those of Airdrop, although a better definition of boundary conditions, such as ice thickness and internal thermal conditions, would be needed for this.

Our findings highlight the complex behaviour and dynamics of glaciers in the Canadian Arctic and emphasize the fact that not all glaciers respond in the same way to external forcing. Comprehensive studies of dynamic instabilities in the Canadian Arctic, which have been scarcely analyzed, along with additional research on the role of long-term mass balance trends in driving glacier dynamics could help identify the range of factors causing the observed variety of glacier dynamic behaviour and improve our understanding of how these dynamics might evolve in a changing climate.

Acknowledgements

We thank the Natural Sciences and Engineering and Research Council, the ArcticNet Network of Centres of Excellence Canada, the University of Manitoba, and the University of Ottawa for supporting this work. We also acknowledge the National Air Photo library for their help with acquiring some of the historical aerial photographs for Airdrop Glacier and GAMMA Remote Sensing for their help with the processing of ERS data.

Article information

History dates

Received: 18 October 2022
Accepted: 28 July 2023
Accepted manuscript online: 31 August 2023
Version of record online: 27 October 2023

Copyright

Data availability

Data generated or analyzed during this study are available from the corresponding author upon reasonable request. Air photos used in this study are available from the National Air Photo Library, Ottawa, Canada. All satellite imagery used in this study is publicly available from the data sources listed in the methods.

Author information

Author ORCIDs

Benoît Lauzon https://orcid.org/0000-0001-6350-0115
Luke Copland https://orcid.org/0000-0001-5374-2145
Wesley Van Wychen https://orcid.org/0000-0002-4275-6768
William Kochtitzky https://orcid.org/0000-0001-9487-1509
Robert McNabb https://orcid.org/0000-0003-0016-493X

Author notes

Luke Copland served as Associate Editor at the time of manuscript review and acceptance and did not handle peer review and editorial decisions regarding this manuscript.

Author contributions

Conceptualization: BL, LC
Data curation: BL
Formal analysis: BL
Funding acquisition: LC, WVW
Investigation: BL, WK
Methodology: BL, LC, WVW, RM
Project administration: LC
Resources: LC, WVW
Software: BL, WVW, WK, RM
Supervision: LC
Validation: BL, LC
Visualization: BL
Writing – original draft: BL
Writing – review & editing: BL, LC, WVW, WK, RM

Competing interests

The authors declare there are no competing interests.

References

Bahr, D.B., Pfeffer, W.T., Sassolas, C., and Meier, M.F. 1998. Response time of glaciers as a function of size and mass balance: 1. Theory. Journal of Geophysical Research, **103**(B5): 9777–9782. doi:10.1029/98JB00507.

Barry, R.G., and Hall-McKim, E.A. 2019. Polar environments and global change. Cambridge University Press, Cambridge. doi:10.1017/9781108399708.

Benn, D.I., Fowler, A.C., Hewitt, I., and Sevestre, H. 2019a. A general theory of glacier surges. Journal of Glaciology, **65**(253): 701–716. doi:10.1017/jog.2019.62.

Benn, D.I., Jones, R.L., Luckman, A., Fürst, J.J., Hewitt, I., and Sommer, C. 2019b. Mass and enthalpy budget evolution during the surge of a polythermal glacier: a test of theory. Journal of Glaciology, **65**(253): 717–731. doi:10.1017/jog.2019.63.

Ciracì, E., Velicogna, I., and Swenson, S. 2020. Continuity of the mass loss of the world's glaciers and ice caps from the GRACE and GRACE Follow-On missions. Geophysical Research Letters, **47**(9): 1–11. doi:10.1029/2019GL086926.

Cogley, J.G., Adams, W.P., and Ecclestone, M.A. 2011. Half a century of measurements of glaciers on Axel Heiberg Island, Nunavut, Canada. Arctic, **64**(3): 371–375. doi:10.14430/arctic4127.

Cogley, J.G., Adams, W.P., Ecclestone, M.A., Jung-Rothenhäusler, F., and Ommanney, C.S.L. 1996a. Mass balance of white glacier, Axel Heiberg Island, NWT, Canada, 1960–91. Journal of Glaciology, **42**(142): 548–563. doi:10.3189/S0022143000003531.

Cogley, J.G., and Adams, W. 2000. Remote-sensing resources for monitoring glacier fluctuations on Axel Heiberg Island. Arctic, **53**(3): 248–259. doi:10.14430/arctic856.

Cogley, J.G., Ecclestone, M.A., and Adams, W.P. 1996b. Fluctuations of the terminuses of White and Thompson Glaciers, Axel Heiberg Island, NWT, Canada. In Eastern Snow Conference Proceedings. **Vol. 53**. pp. 83–94.

Copland, L., Sharp, M., and Dowdeswell, J. 2003. The distribution and flow characteristics of surge-type glaciers in the Canadian High Arctic. Annals of Glaciology, **36**(1): 73–81. doi:10.3189/172756403781816301.

Dalton, A., Van Wychen, W., Copland, L., Gray, L., and Burgess, D. 2022. Seasonal and multiyear flow variability on the Prince of Wales Icefield, Ellesmere Island: 2009–2019. Journal of Geophysical Research: Earth Surface, **127**(4): e2021JF006501. doi:10.1029/2021JF006501.

Debella-Gilo, M., and Kääb, A. 2011. Sub-pixel precision image matching for measuring surface displacements on mass movements using normalized cross-correlation. Remote Sensing of Environment, **115**(1): 130–142. doi:10.1016/j.rse.2010.08.012.

Dolgoushin, L.D., and Osipova, G.B. 1975. Glacier surges and the problem of their forecasting (Symposium at Moscow 1971 – Snow and Ice). IASH Publications **104**: 292–304.

Dowdeswell, J.A., and Benham, T.J. 2003. A surge of Perseibreen, Svalbard, examined using aerial photography and ASTER high resolution satellite imagery. Polar Research, **22**(2): 373–383. doi:10.3402/polar.v22i2.6466.

Dowdeswell, J.A., Hamilton, G.S., and Hagen, J.O. 1991. The duration of the active phase on surge-type glaciers: contrasts between Svalbard and other regions. Journal of Glaciology, **37**(127): 388–400. doi:10.3189/S0022143000005827.

Dunse, T., Schellenberger, T., Hagen, J.O., Kääb, A., Schuler, T.V., and Reijmer, C.H. 2015. Glacier-surge mechanisms promoted by a hydro-thermodynamic feedback to summer melt. Cryosphere, **9**(1): 197–215. doi:10.5194/tc-9-197-2015.

Farinotti, D., Immerzeel, W.W., de Kok, R.J., Quincey, D.J., and Dehecq, A. 2020. Manifestations and mechanisms of the Karakoram glacier Anomaly. Nature Geoscience, **13**(1): 8–16. doi:10.1038/s41561-019-0513-5.

Flink, A.E., Noormets, R., Kirchner, N., Benn, D.I., Luckman, A., and Lovell, H. 2015. The evolution of a submarine landform record following recent and multiple surges of Tunabreen glacier, Svalbard. Quaternary Science Reviews, **108:** 37–50. doi:10.1016/j.quascirev.2014.11.006.

Flowers, G.E. 2015. Modelling water flow under glaciers and ice sheets. Proceedings of the Royal Society A: Mathematical, Physical and Engineering Sciences, **471**(2176): 20140907. doi:10.1098/rspa.2014.0907.

Flowers, G.E., Roux, N., Pimentel, S., and Schoof, C.G. 2011. Present dynamics and future prognosis of a slowly surging glacier. Cryosphere, **5**(1): 299–313. doi:10.5194/tc-5-299-2011.

Frappé, T.P., and Clarke, G.K. 2007. Slow surge of Trapridge Glacier, Yukon Territory, Canada. Journal of Geophysical Research, **112**(F3): F03S32. doi:10.1029/2006JF000607.

Gardner, A., Fahnestock, M., and Scambos, T. 2022. MEaSUREs ITS_LIVE Regional Glacier and Ice Sheet Surface Velocities, Version 1. NASA National Snow and Ice Data Center Distributed Active Archive Center. doi:10.5067/6II6VW8LLWJ7.

Gardner, A.S., Moholdt, G., Scambos, T., Fahnstock, M., Ligtenberg, S., Van Den Broeke, M., et al. 2018. Increased West Antarctic and unchanged East Antarctic ice discharge over the last 7 years. Cryosphere, **12**(2): 521–547. doi:10.5194/tc-12-521-2018.

Gardner, A.S., Moholdt, G., Wouters, B., Wolken, G.J., Burgess, D.O., Sharp, M.J., et al. 2011. Sharply increased mass loss from glaciers and ice caps in the Canadian Arctic Archipelago. Nature, **473**(7347): 357–360. doi:10.1038/nature10089.

Girod, L., Nuth, C., Kääb, A., McNabb, R., and Galland, O. 2017. MMASTER: improved ASTER DEMs for elevation change monitoring. Remote Sensing, **9**(7): 704. doi:10.3390/rs9070704.

Haga, O.N., McNabb, R., Nuth, C., Altena, B., Schellenberger, T., and Kääb, A. (2020). From high friction zone to frontal collapse: dynamics of an ongoing tidewater glacier surge, Negribreen, Svalbard. Journal of Glaciology, **66**(259): 742–754. doi:10.1017/jog.2020.43.

Harcourt, W.D., Palmer, S.J., Mansell, D.T., Le Brocq, A., Bartlett, O., Gourmelen, N., et al. 2020. Subglacial controls on dynamic thinning at Trinity-Wykeham Glacier, Prince of Wales Ice Field, Canadian Arctic. International Journal of Remote Sensing, **41**(3): 1191–1213. doi:10.1080/01431161.2019.1658238.

Hugonnet, R., McNabb, R., Berthier, E., Menounos, B., Nuth, C., Girod, L., et al. 2021. Accelerated global glacier mass loss in the early twenty-first century. Nature, **592**(7856): 726–731. doi:10.1038/s41586-021-03436-z.

Huss, M. 2013. Density assumptions for converting geodetic glacier volume change to mass change. Cryosphere, **7**(3): 877–887. doi:10.5194/tc-7-877-2013.

Iken, A., and Bindschadler, R.A. 1986. Combined measurements of subglacial water pressure and surface velocity of Findelengletscher, Switzerland: conclusions about drainage system and sliding mechanism. Journal of Glaciology, **32**(110): 101–119. doi:10.1017/S0022143000006936.

Jiskoot, H. 2011. Glacier surging. In Singh, Singh, and Haritashya, (Eds). Encyclopedia of snow, ice and glaciers. Springer, Dordrecht. pp. 415–428. doi:10.1007/978-90-481-2642-2_559.

Jóhannesson, T., Raymond, C., and Waddington, E.D. 1989. Time–scale for adjustment of glaciers to changes in mass balance. Journal of Glaciology, **35**(121): 355–369. doi:10.3189/S002214300000928X.

Kochtitzky, W., and Copland, L. 2022. Retreat of Northern hemisphere marine-terminating glaciers, 2000–2020. Geophysical Research Letters, **49**(3): e2021GL096501. doi:10.1029/2021gl096501.

Kochtitzky, W., Copland, L., Wohlleben, T., Iqaluk, P., Girard, C., Vincent, W.F., and Culley, A.I. 2023. Slow change since the Little Ice Age at a far northern glacier with the potential for system reorganization: Thores Glacier, northern Ellesmere Island, Canada. Arctic Science, **9**(2): 451–464. doi:10.1139/as-2022-0012.

Kochtitzky, W., Jiskoot, H., Copland, L., Enderlin, E., McNabb, R., Kreutz, K., et al. 2019. Terminus advance, kinematics and mass redistribution during eight surges of Donjek Glacier, St. Elias Range, Canada, 1935 to 2016. Journal of Glaciology, **65**(252): 565–579. doi:10.1017/jog.2019.34.

Koerner, R.M. 2005. Mass balance of glaciers in the Queen Elizabeth Islands, Nunavut, Canada. Annals of Glaciology, **42**: 417–423. doi:10.3189/172756405781813122.

Lauzon, B., Copland, L., Van Wychen, W., Kochtitzky, W., McNabb, R., and Dahl-Jensen, D. 2023. Dynamics throughout a complete surge of Iceberg Glacier on western Axel Heiberg Island, Canadian High Arctic. Journal of Glaciology, 1–18. doi:10.1017/jog.2023.20.

Lenaerts, J.T., van Angelen, J.H., van den Broeke, M.R., Gardner, A.S., Wouters, B., and van Meijgaard, E. 2013. Irreversible mass loss of Canadian Arctic Archipelago glaciers. Geophysical Research Letters, **40**(5): 870–874. doi:10.1002/grl.50214.

Luckman, A., Murray, T., and Strozzi, T. 2002. Surface flow evolution throughout a glacier surge measured by satellite radar interferometry. Geophysical Research Letters, **29**(23): 10–11. doi:10.1029/2001GL014570.

Lv, M., Guo, H., Yan, J., Wu, K., Liu, G., Lu, X., et al. 2020. Distinguishing glaciers between surging and advancing by remote sensing: a case study in the Eastern Karakoram. Remote Sensing, **12**(14): 2297. doi:10.3390/rs12142297.

Maurer, J., and Rupper, S. 2015. Tapping into the Hexagon spy imagery database: a new automated pipeline for geomorphic change detection. ISPRS Journal of Photogrammetry and Remote Sensing, **108**: 113–127. doi:10.1016/j.isprsjprs.2015.06.008.

McNabb, R., Girod, L., Nuth, C., and Kääb, A. 2020. An open-source toolset for automated processing of historic spy photos: sPyMicMac. *In* EGU General Assembly Conference Abstracts, 4–8 May 2020, European Geoscience Union, Munich. p. 11150. doi:10.5194/egusphere-egu2020-11150.

Medrzycka, D., Copland, L., Van Wychen, W., and Burgess, D. 2019. Seven decades of uninterrupted advance of Good Friday Glacier, Axel Heiberg Island, Arctic Canada. Journal of Glaciology, **65**(251): 440–452. doi:10.1017/jog.2019.21.

Meier, M.F., and Post, A. 2011. What are glacier surges? Geophysical Research Letters, **38**(4). doi:10.1029/2011GL049004.

Millan, R., Mouginot, J., and Rignot, E. 2017. Mass budget of the glaciers and ice caps of the Queen Elizabeth Islands, Canada, from 1991 to 2015. Environmental Research Letters, **12**(2): 024016. doi:10.1088/1748-9326/aa5b04.

Miller, G.H., Geirsdóttir, Á., Zhong, Y., Larsen, D.J., Otto-Bliesner, B.L., Holland, M.M., et al. 2012. Abrupt onset of the Little Ice Age triggered by volcanism and sustained by sea-ice/ocean feedbacks. Geophysical Research Letters, **39**(2). doi:10.1029/2011GL050168.

Moore, J.J., Hughen, K.A., Miller, G.H., and Overpeck, J.T. 2001. Little Ice Age recorded in summer temperature reconstruction from vared sediments of Donard Lake, Baffin Island, Canada. Journal of Paleolimnology, **25**: 503–517. doi:10.1023/A:1011181301514.

Mortimer, C.A., Sharp, M., and Van Wychen, W. 2018. Influence of recent warming and ice dynamics on glacier surface elevations in the Canadian High Arctic, 1995–2014. Journal of Glaciology, **64**(245): 450–464. doi:10.1017/jog.2018.37.

Murray, T., James, T.D., Macheret, Y., Lavrentiev, I., Glazovsky, A., and Sykes, H. 2012. Geometric changes in a tidewater glacier in Svalbard during its surge cycle. Arctic, Antarctic, and Alpine Research, **44**(3): 359–367. doi:10.1657/1938-4246-44.3.359.

Murray, T., Strozzi, T., Luckman, A., Jiskoot, H., and Christakos, P. 2003. Is there a single surge mechanism? Contrasts in dynamics between glacier surges in Svalbard and other regions. Journal of Geophysical Research, **108**(B5). doi:10.1029/2002JB001906.

Nick, F.M., Vieli, A., Howat, I.M., and Joughin, I. 2009. Large-scale changes in Greenland outlet glacier dynamics triggered at the terminus. Nature Geoscience, **2**(2): 110–114. doi:10.1038/ngeo394.

Noël, B., van de Berg, W.J., Lhermitte, S., Wouters, B., Schaffer, N., and van den Broeke, M.R. 2018. Six decades of glacial mass loss in the Canadian Arctic Archipelago. Journal of Geophysical Research: Earth Surface, **123**(6): 1430–1449. doi:10.1029/2017JF004304.

Nuth, C., and Kääb, A. 2011. Co-registration and bias corrections of satellite elevation data sets for quantifying glacier thickness change. Cryosphere, **5**(1): 271–290. doi:10.5194/tc-5-271-2011.

Ommanney, C.S.L. 1969. A study in glacier inventory: the ice masses of Axel Heiberg Island, Canadian Arctic Archipelago. McGill University, Montréal, QC (Axel Heiberg Island Research Reports Glaciology 3).

Paul, F., Barrand, N.E., Baumann, S., Berthier, E., Bolch, T., Casey, K., et al. 2013. On the accuracy of glacier outlines derived from remote-sensing data. Annals of Glaciology, **54**(63): 171–182. doi:10.3189/2013AoG63A296.

Pfeffer, W.T. 2007. A simple mechanism for irreversible tidewater glacier retreat. Journal of Geophysical Research, **112**(F3): 1–12. doi:10.1029/2006JF000590.

Pfeffer, W.T., Arendt, A.A., Bliss, A., Bolch, T., Cogley, J.G., Gardner, A.S., et al. 2014. The Randolph Glacier Inventory: a globally complete inventory of glaciers. Journal of Glaciology, **60**(221): 537–552. doi:10.3189/2014JoG13J176.

Pfeffer, W.T., Sassolas, C., Bahr, D.B., and Meier, M.F. 1998. Response time of glaciers as a function of size and mass balance: 2. Numerical experiments. Journal of Geophysical Research, **103**(B5): 9783–9789. doi:10.1029/98JB00508.

Raper, S.C., and Braithwaite, R.J. 2009. Glacier volume response time and its links to climate and topography based on a conceptual model of glacier hypsometry. Cryosphere, **3**(2): 183–194. doi:10.5194/tc-3-183-2009.

RGI Consortium. 2017. Randolph Glacier Inventory—a dataset of global glacier outlines, version 6.0. National Snow and Ice Data Center. doi:10.7265/4m1f-gd79.

Rolstad, C., Amlien, J., Hagen, J.O., and Lundén, B. 1997. Visible and near-infrared digital images for determination of ice velocities and surface elevation during a surge on Osbornebreen, a tidewater glacier in Svalbard. Annals of Glaciology, **24:** 255–261. doi:10.3189/S026030550001226X.

Rupnik, E., Daakir, M., and Pierrot Deseilligny, M. 2017. MicMac–a free, open-source solution for photogrammetry. Open Geospatial Data, Software and Standards, **2**(1): 1–9. doi:10.1186/s40965-017-0027-2.

Schaffer, N., Copland, L., and Zdanowicz, C. 2017. Ice velocity changes on penny ice cap, baffin island, since the 1950s. Journal of Glaciology, **63**(240): 716–730. doi:10.1017/jog.2017.40.

Sevestre, H., and Benn, D.I. 2015. Climatic and geometric controls on the global distribution of surge-type glaciers: implications for a unifying model of surging. Journal of Glaciology, **61**(228): 646–662. doi:10.3189/2015JoG14J136.

Sevestre, H., Benn, D.I., Luckman, A., Nuth, C., Kohler, J., Lindbäck, K., et al. 2018. Tidewater glacier surges initiated at the terminus. Journal of Geophysical Research: Earth Surface, **123**(5): 1035–1051. doi:10.1029/2017JF004358.

Strozzi, T., Paul, F., Wiesmann, A., Schellenberger, T., and Kääb, A. 2017. Circum-Arctic changes in the flow of glaciers and ice caps from satellite SAR data between the 1990 s and 2017. Remote Sensing, **9**(9): 947. doi:10.3390/rs9090947.

Sund, M., Eiken, T., Hagen, J.O., and Kääb, A. 2009. Svalbard surge dynamics derived from geometric changes. Annals of Glaciology, **50**(52): 50–60. doi:10.3189/172756409789624265.

Thomson, L., and Copland, L. 2016. White Glacier 2014, Axel Heiberg Island, Nunavut: mapped using structure from motion methods. Journal of Maps, **12**(5): 1063–1071. doi:10.1080/17445647.2015.1124057.

Thomson, L.I., and Copland, L. 2017. Multi-decadal reduction in glacier velocities and mechanisms driving deceleration at polythermal White Glacier, Arctic Canada. Journal of Glaciology, **63**(239): 450–463. doi:10.1017/jog.2017.3.

Thomson, L.I., Osinski, G.R., and Ommanney, C.S.L. 2011. Glacier change on Axel Heiberg Island, Nunavut, Canada. Journal of Glaciology, **57**(206): 1079–1086. doi:10.3189/002214311798843287.

Thomson, L.I., Zemp, M., Copland, L., Cogley, J.G., and Ecclestone, M.A. 2017. Comparison of geodetic and glaciological mass budgets for White Glacier, Axel Heiberg Island, Canada. Journal of Glaciology, **63**(237): 55–66. doi:10.1017/jog.2016.112.

Van Wychen, W., Burgess, D., Kochtitzky, W., Nikolic, N., Copland, L., and Gray, L. 2021. RADARSAT-2 derived glacier velocities and dynamic discharge estimates for the Canadian High Arctic: 2015–2020. Canadian Journal of Remote Sensing, **46**(6): 695–714. doi:10.1080/07038992.2020.1859359.

Van Wychen, W., Burgess, D.O., Gray, L., Copland, L., Sharp, M., Dowdeswell, J.A., et al. 2014. Glacier velocities and dynamic ice discharge from the Queen Elizabeth Islands, Nunavut, Canada. Geophysical Research Letters, **41**(2): 484–490. doi:10.1002/2013GL058558.

Van Wychen, W., Davis, J., Burgess, D.O., Copland, L., Gray, L., Sharp, M., et al. 2016. Characterizing interannual variability of glacier dynamics and dynamic discharge (1999–2015) for the ice masses of Ellesmere and Axel Heiberg Islands, Nunavut, Canada. Journal of Geophysical Research: Earth Surface, **121**(1): 39–63. doi:10.1002/2015JF003708.

Van Wychen, W., Davis, J., Copland, L., Burgess, D.O., Gray, L., Sharp, M., et al. 2017. Variability in ice motion and dynamic discharge from Devon Ice Cap, Nunavut, Canada. Journal of Glaciology, **63**(239): 436–449. doi:10.1017/jog.2017.2.

Van Wychen, W., Hallé, D.A., Copland, L., and Gray, L. 2022. Anomalous surface elevation, velocity and area changes of Split Lake Glacier, western Prince of Wales Icefield, Canadian High Arctic. Arctic Science. doi:10.1139/AS-2021-0039.

Van Wyk de Vries, M. 2021a. Glacier image velocimetry (GIV), Zenodo. doi:10.5281/zenodo.4624831.

Van Wyk de Vries, M. 2021b. Glacier image velocimetry (GIV) app. doi:10.5281/zenodo.4147589.

Van Wyk de Vries, M., and Wickert, A.D. 2021. Glacier image velocimetry: an open-source toolbox for easy and rapid calculation of high-resolution glacier velocity fields. Cryosphere, **15**(4): 2115–2132. doi:10.5194/tc-15-2115-2021.

Zekollari, H., Huss, M., and Farinotti, D. 2020. On the imbalance and response time of glaciers in the European Alps. Geophysical Research Letters, **47**(2): e2019GL085578. doi:10.1029/2019GL085578.